Hydrothermal evolution and origin of the Suixian molybdenum deposit in the Tongbai orogenic belt, China: Constraints from geology, fluid inclusions and multiple isotopes (H O C S Pb)

Pan-Pan Niu, Shao-Yong Jiang, Wen-Tian Li, Pei-Long Cui, Yi-Chun Chen, Manuel Muñoz

Ore Geology Reviews 148 (2022) 105036

Contents lists available at ScienceDirect

Ore Geology Reviews

journal homepage: www.elsevier.com/locate/oregeorev

Hydrothermal evolution and origin of the Suixian molybdenum deposit in the Tongbai orogenic belt, China: Constraints from geology, fluid inclusions and multiple isotopes (H—O—C—S—Pb)

Pan-Pan Niu [a,b], Shao-Yong Jiang [a,b,*], Wen-Tian Li [a], Pei-Long Cui [c], Yi-Chun Chen [c], Manuel Muñoz [d]

[a] State Key Laboratory of Geological Processes and Mineral Resources, Collaborative Innovation Center for Exploration of Strategic Mineral Resources, School of Earth Resources, China University of Geosciences, Wuhan 430074, China
[b] Key Laboratory of Geological Survey and Evaluation of Ministry of Education, China University of Geosciences, Wuhan 430074, China
[c] Eighth Geological Brigade of Hubei Geological Bureau, Xiangyang 441000, China
[d] Geosciences Montpellier, University of Montpellier, CNRS, Montpellier 34095, France

ARTICLE INFO

Keywords:
Fluid inclusions
S–C–H–O–Pb isotopes
Mo deposit
Tongbai orogen

ABSTRACT

The Suixian Mo deposit is a recently discovered deposit in the northern Hubei Province, Tongbai orogen. The Mo orebodies of this deposit are all hosted in the metamorphic rocks (leuco-gneiss, amphibolite and marble) of the Neoproterozoic Tianwangzhai Group, and these orebodies have no direct contact with the granite surrounding the host rocks. The mineralization types are dominated by disseminated ore and fine Mo-bearing quartz-sulfide veins. Hydrothermal alteration consists of abundant feldspathization, epidotization and chloritization, together with less garnetization, tremolitization, and muscovitization. A detailed study on fluid inclusions and multiple isotope (C—H—O—S—Pb) analyses, together with geologic features, are carried out to investigate the fluid composition, fluid origin and evolution, the source of ore-forming materials, and the ore genetic type. In line with microthermometric measurements and laser Raman analysis on fluid inclusions from three hydrothermal stages, the ore-forming fluid in this deposit is characterized by medium–high temperatures and salinities, as well as richness in CO_2 and CH_4. Three hydrothermal stages are identified in this deposit, including (I) feldspar-quartz-amphibole-muscovite stage, (II) quartz-sulfides stage, and (III) quartz-calcite-scheelite-fluorite stage. From stages I, II to III, the temperatures change from 290 to 354 °C, through 229–312 °C, to 173–269 °C, with decreasing salinities of 12.6 to 16.3 wt% NaCl equiv., 4.5 to 13.4 wt% NaCl equiv., and 0.2 to 6.9 wt% NaCl equiv., respectively. Most of sulfur isotope data of sulfides (chalcopyrite, pyrite, pyrrhotite and molybdenite) show a narrow $\delta^{34}S$ range from −2.0 to 3.0 ‰, suggesting a dominant magmatic source, but some data show either positive or negative values ($\delta^{34}S$: −13.3 to −10.6 ‰ and 9.8 to 11.2 ‰) which may indicate small contribution from the restricted wall rocks. The Pb isotope data (molybdenite, pyrite and pyrrhotite: $^{206}Pb/^{204}Pb$: 17.239 to 18.483; $^{207}Pb/^{204}Pb$: 15.378 to 15.717; $^{208}Pb/^{204}Pb$: 37.889 to 38.850) imply that the lead of sulfides pertains to a mixture of magma (derived from the lower crust) and upper crustal materials (host metamorphic rocks). Based on evident CO_2 and CH_4 in fluid inclusions, the gradually depleted carbon isotopic compositions ($\delta^{13}C$: −5.4 to −9.9 ‰ at stage I, −14.8 to −19.7 ‰ at stage II, and −17.0 to −24.2 ‰ at stage III) and the H—O isotope data, it is suggested that the ore-forming fluids were mainly magmatic fluids with mixture of some organic-containing water, and the thermochemical reaction between the fluids and organic matters (e.g., CH_4) from host metamorphic rocks and fluid immiscibility are two important mechanisms for Mo mineralization. Compared with typical Mo deposits in the same orogen, the Suixian Mo deposit belongs to the magmatic hydrothermal vein-type deposit associated with intrusions rather than porphyry or skarn type deposit.

* Corresponding author at: Key Laboratory of Geological Survey and Evaluation of Ministry of Education, China University of Geosciences, Wuhan 430074, China.
E-mail address: shyjiang@cug.edu.cn (S.-Y. Jiang).

https://doi.org/10.1016/j.oregeorev.2022.105036
Received 12 January 2022; Received in revised form 13 July 2022; Accepted 18 July 2022
Available online 22 July 2022

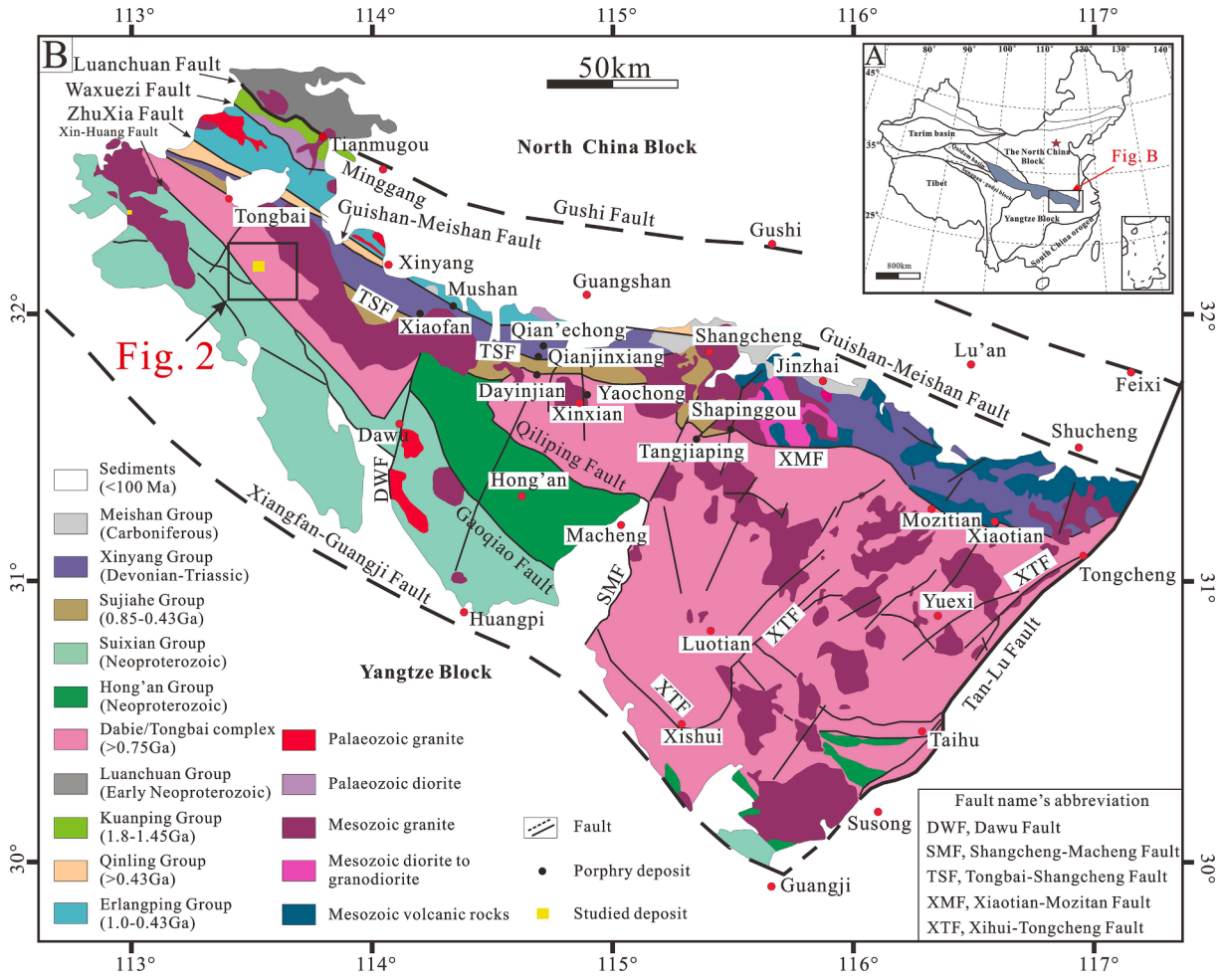

Fig. 1. Generalized geological map of the Tongbai-Dabie orogen in China, showing the position of the Suixian Mo deposit and these porphyry type Mo deposits in the Dabie orogen (modified after Wang et al., 2009).

1. Introduction

The Tongbai-Dabie orogen is a part of the EW-trending Qinling-Dabie orogens, formed by continental collision between the Yangtze Block and North China Block in the Mesozoic period (Fig. 1A; Gao et al., 2014, 2016; Ni et al., 2015; Yang et al., 2017). The Tongbai-Dabie orogen is well-known for its well-preserved ultrahigh-pressure/high pressure (UHP/HP) metamorphic rocks and huge Mesozoic porphyry-type Mo resource (>3 Mt Mo), for example the Shapinggou, Qian'echong, and Yaochong Mo deposits (Fig. 1B; Mi et al., 2015a; Chen et al., 2017a, b; Yang et al., 2017). The granitoids related to molybdenum mineralization intruded into the Tongbai-Dabie area between 143 and 117 Ma based on zircon U-Pb dating (Gao et al., 2016). The granitoids formed 130 Ma ago derived from partial melting of the thickened crust, and the granitoids formed 130 Ma later originated from partial melting of the delaminated lower crust (He et al., 2011; Gao et al., 2016; Ren et al., 2018). The molybdenite Re-Os dating concludes that these Mo mineralizations also occurred in two periods: 148–138 Ma and 131–112 Ma (Mao et al., 2011; Chen et al., 2017a).

The Tongbai-Dabie orogen includes eastern Shaanxi, northern Hubei, northeastern Anhui and southern Henan provinces (Mao et al., 2011). A series of large and giant Mo deposits have been discovered in Henan and Anhui provinces, but no economic Mo deposits have been found in the Hubei Province previously (e.g., Mao et al., 2011; Gao et al., 2014, 2016; Cao et al., 2016; Deng et al., 2017; Wang et al., 2014b; Ni et al., 2012, 2014,2015; Liu et al., 2017a; Wang et al., 2017). The Suixian Mo deposit, located in the Tongbai complex, is the only one economic Mo deposit in Hubei Province, which was found by a 1:200,000 geochemical anomaly inspection of the Eighth Geological Brigade of Hubei Province (Chen et al., 2017c). The Suixian Mo deposit contains four ore blocks: Shuangbaojian, Baiguoshu, Huangjiagou and Jianshuitian (Fig. 2). At present, sixteen proven orebodies from Huangjiagou and Jianshuitian host 100,000 t Mo metal resource with an average grade of 0.084 % (Chen et al., 2017c), manifesting that the Suixian Mo deposit is a middle-sized Mo deposit and may have a potential for large deposit with further exploration work. Niu et al. (2017) reported a 131.3 ± 2.5 Ma Re-Os age of molybdenite from the Huangjiagou ore block. In the same year, Chen et al. (2017c) determined a U-Pb age of 137.6 ± 1.6 Ma for the Dongyuemiao granite (close to Mo-bearing metamorphic rocks), and a Re-Os isochron age of 137.0 ± 8.1 Ma from seven molybdenite samples. Based on above similar ages between Mo mineralization and the Dongyuemiao granite (Fig. 3A, B), the Suixian Mo deposit was classified as porphyry or skarn type deposits (Chen et al., 2017a; Niu et al., 2017). However, the Mo mineralization is hosted only in the metamorphic rocks (Tianwangzhai Group) and is not in direct contact with the surrounding granites, which is different from the typical porphyry and skarn type deposits (Wu et al., 2015; Dai et al., 2018). In order to solve the above problem in this study, we (1) document the Mo mineralization characteristics and its relationship; (2) study the characteristics of ore-forming fluids by fluid inclusions; (3) trace the origin and evolution of ore-forming fluids by the C—H—O isotopes; and (4) use sulfur and lead isotopes to track the sources of ore-forming materials, so as to determine the ore-forming process and ore genesis of the Suixian Mo deposit.

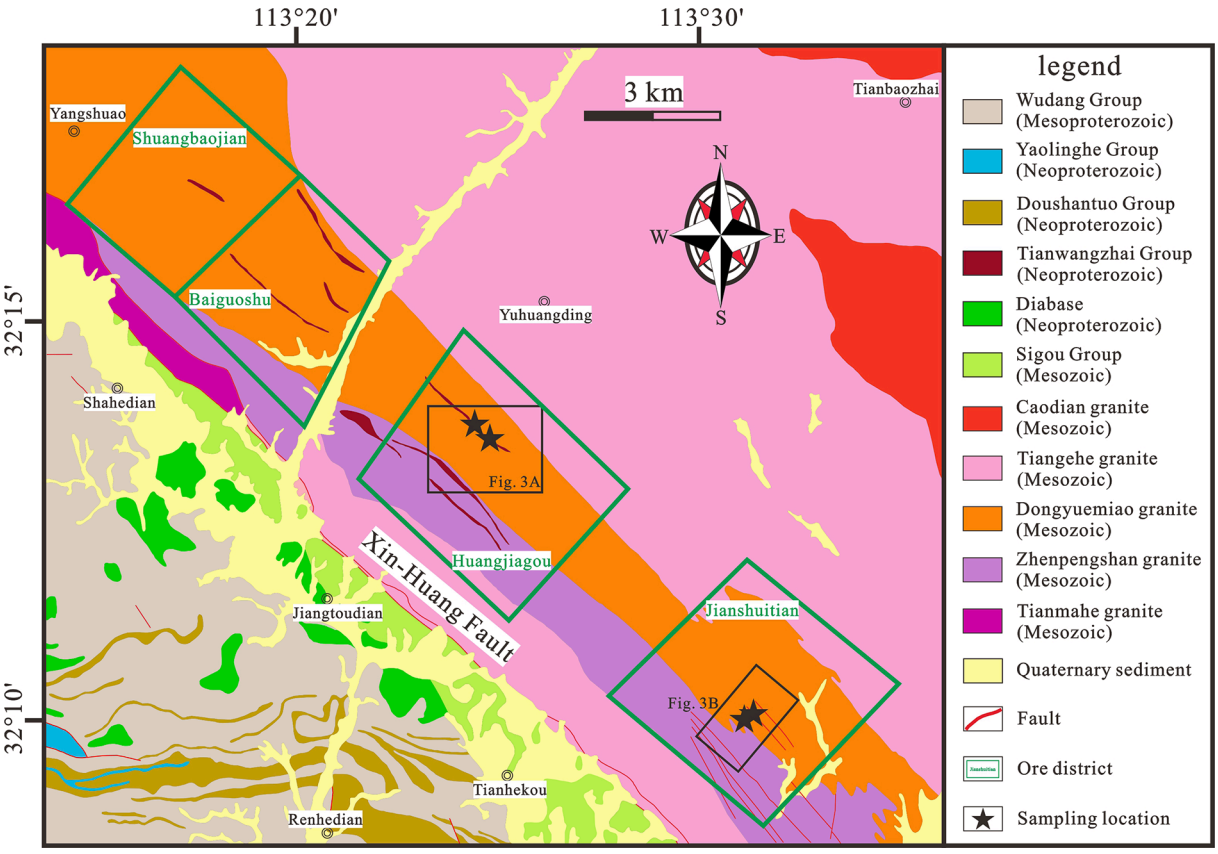

Fig. 2. Brief geological map of the Tongbai complex and the Suixian Mo deposits (modified after Xiang et al., 2019).

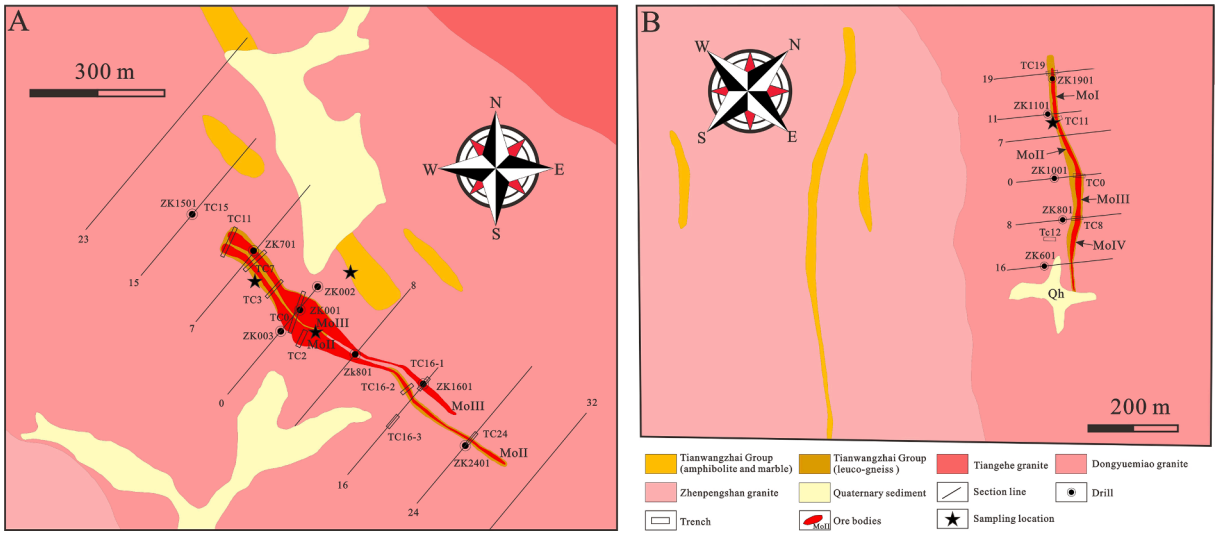

Fig. 3. Geological sketch of the Huangjiagou and Jianshuitian ore blocks in the Suixian Mo deposit (modified after Chen et al., 2017c).

2. Regional geology

2.1. Tectonic setting and structural framework

The Tongbai-Dabie orogen spreads along with a near-EW direction, gripped by the North China and Yangtze Blocks (Fig. 1A). This orogen links to the western Qinling orogen through the Nanyang Basin and the eastern Sulu orogen by the Tan-Lu Fault (Fig. 1B; Mi et al., 2015b; Gao et al., 2016; Gao et al., 2018; Li et al., 2018). In general, the NW and NE to NNE trending faults constitute the tectonic pattern of this orogen (Fig. 1B; Wang et al., 2017; Yang et al., 2017). The former is represented by the Luanchuan-Gushi Fault, Guishan-Meishan Fault, Tongbai-Shangcheng Fault and Xiaotian-Mozitian Fault, and the latter includes the Dawu Fault, Doushanhe Fault and Shang-Ma Fault (Fig. 1B).

2.2. Strata

The tectonostratigraphy of the Tongbai-Dabie orogen can be divided in two parts by the Guishan-Meishan Fault (Fig. 1B): (1) To the north: the Mesoproterozoic Kuangping Group, Paleozoic-Neoproterozoic

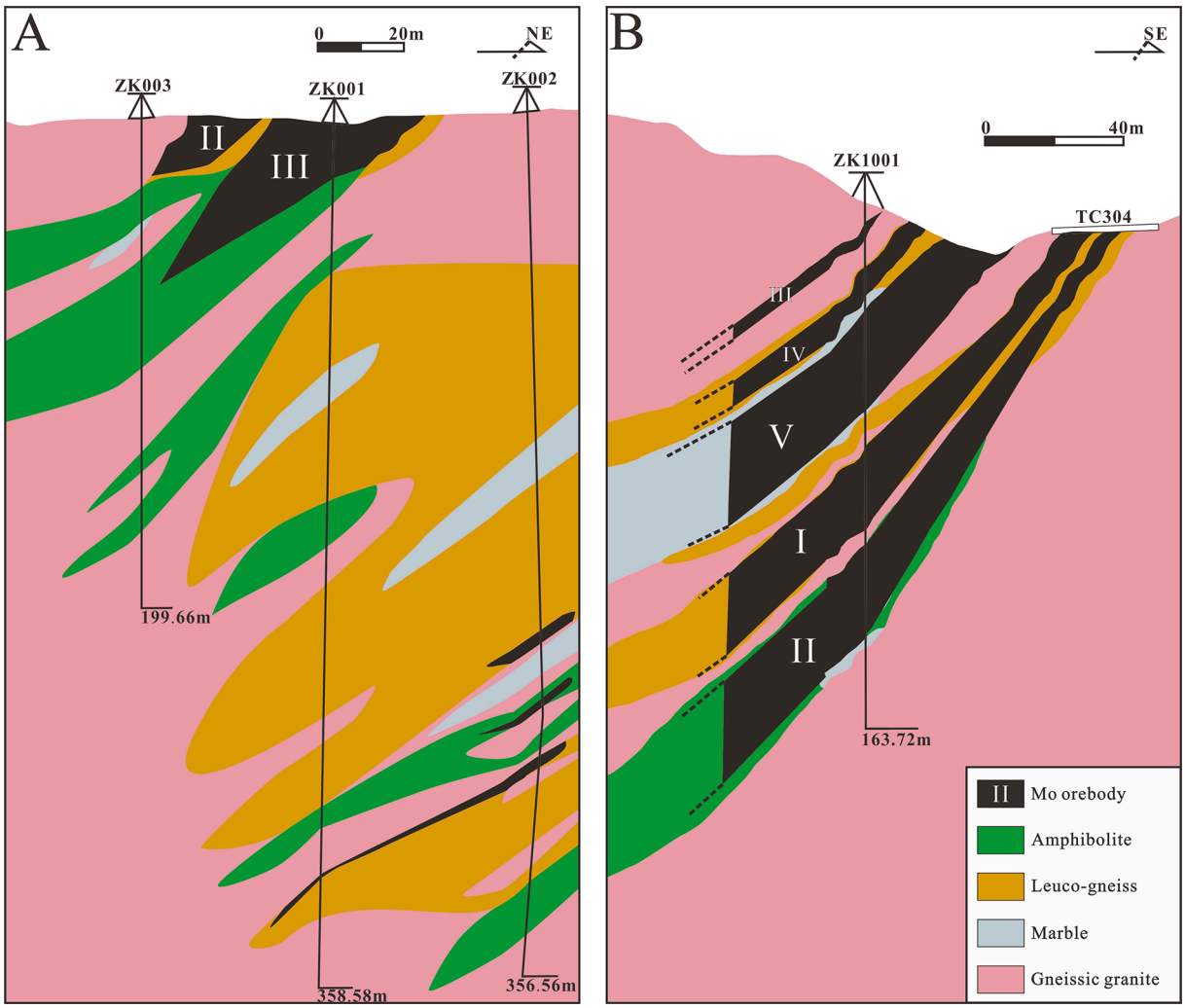

Fig. 4. Cross sections of the Mo orebody at Huangjiagou (A) and Jianshuitian (B) ore blocks of the Suixian Mo deposit, also shown the finished trenches and drilling cores (modified after Chen et al., 2017c).

Erlangping Group and mainly Paleoproterozoic Qinling Group are part of the metamorphosed accretion zone during the Paleozoic period (Yang et al., 2013); (2) To the south: the stratigraphic units include the Devonian-Triassic Xinyang Group, Cambrian-Early Neoproterozoic Sujiahe Group, Dabie and Tongbai complex, and Neoproterozoic Hong'an and Suixian Groups (Ni et al., 2015). The Qinling Group is a set of highly metamorphosed magmatic and sedimentary rocks (Wu et al., 2014). The Erlangping Group consists of amphibolites, metamorphosed rhyolites, plagiogneisses and marbles with many metagabbro blocks, showing metamorphism at greenschist to amphibolite facies (Liu et al., 2011). The Kuanping Group comprises mica schists, quartzites, marbles, and amphibolites, protoliths of which were terrigenous sediments, carbonate rocks, and tholeiitic basalts (Niu and Jiang, 2020). The Xinyang Group is a suit of ophiolitic melange (Ni et al., 2015). The Sujiahe Group is composed of amphibolites, felsic gneisses, mica schists, marbles and eclogite enclaves, together with highly strained granites and metagabbro bodies (Liu et al., 2010). The Hong'an Group is dominated by epidote–amphibolite facies volcano-sedimentary rocks (Wang et al., 2009). The Suixian Group is a Neoproterozoic low- to medium-grade metamorphosed volcanic-sedimentary sequence (Wang et al., 2017).

2.3. Intrusion

The igneous rocks in the Tongbai-Dabie orogen is composed of volcanic rocks, granitoids and minor mafic intrusions, which mainly formed in the Paleozoic and Mesozoic eras (Yang et al., 2013; Gao et al., 2014, 2016; Wang et al., 2014a; Liu et al., 2017a). The Paleozoic granitoids are distributed sporadically, while the Mesozoic granitoids dominate the magmatic rocks in the Tongbai-Dabie orogen. The lattermainly formed at 143–117 Ma, belonging to post-collisional rocks, which are divided into two stages: (1) high Sr/Y adakitic granites (>130 Ma) due to partial melting of the thickened lower crust and belong to C-type (continental type) adakites, and (2) low Sr/Y normal granites (<130 Ma) derived from partial melting of the delaminated lower crust and belong to O-type (oceanic type) adakites (Fig. 1B; He et al., 2011, 2013; Niu and Jiang, 2020).

The formation process of the Tongbai complex can be divided into four stages: (1) abundant volcanic and sedimentary rocks were formed in the Neoproterozoic; (2) large-scale Mesozoic granites intruded due to the continental collision; (3) tectonic extension after collision resulted in deformation of the above rocks to form gneiss; and (4) intrusion of some small later intermediate-felsic rocks (e.g., Caodian granite; Fig. 2; Liu et al., 2010; Cui et al., 2012; Zhang et al., 2013; Zhang et al., 2018). The Neoproterozoic volcanic and sedimentary rocks are now dominated by leuco-gneiss (called leptynite and leptite by local geologists), amphibolite and marble, which were classified as the Tianwangzhai Group (Fig. 2; Cui et al., 2012; Niu and Jiang, 2021a). As the main body of the Tongbai complex, the Mesozoic granites were changed into gneissic granites by later deformation and metamorphism, which are divided into several geological units according to lithological differences: (1) the

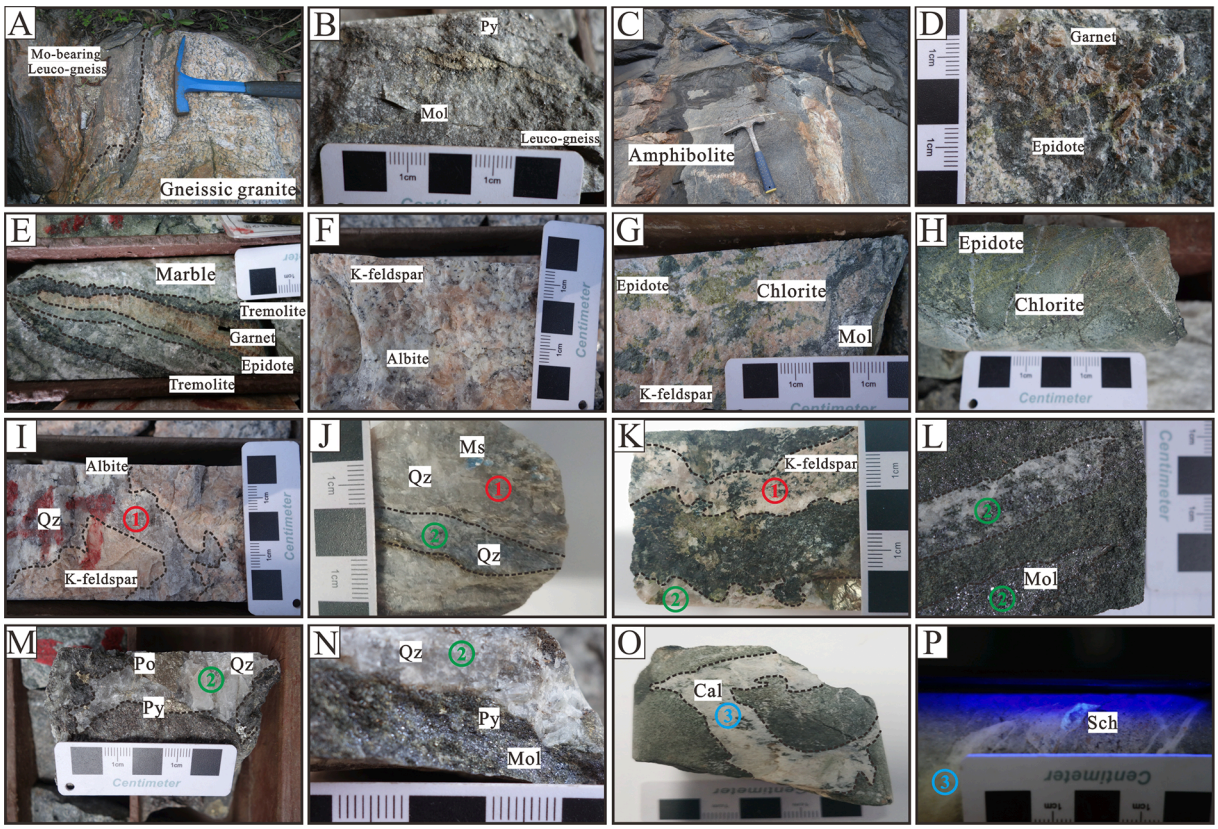

Fig. 5. Representative field and hand specimen photographs from the Suixian Mo deposit. Gneissic granite with ore-bearing leuco-gneiss enclave; (B-C) Ore-bearing leuco-gneiss and amphibolite; (D) Epidotization and garnetization; (E) Epidotization, garnetization and tremolitization in marble; (F) K-feldspathization and albitization; (G) Epidotization, chloritization and K-feldspathization; (H) Epidotization, chloritization and carbonation; (I) Feldspar-quartz- amphibole-muscovite vein (stage I); (J-K) quartz-sulfides vein (stage II) cross-cuts feldspar-quartz- amphibole-muscovite vein (stage I); (L) Molybdenite in quartz-sulfides vein (stage II); (M) Pyrite and pyrrhotite in quartz-sulfides vein (stage II); (N) Pyrite and molybdenite in quartz-sulfides vein (stage II); (O—P) Quartz- calcite-scheelite-fluorite vein (stage III). Abbreviations: Mol- Molybdenite; Py- pyrite; Qz- Quartz; Ms- Muscovite; Po- Pyrrhotite; Cal- Calcite; Sch- Scheelite.

Tiangehe granite: medium-fine grained; (2) the Dongyuemiao granite: medium-coarse-grained; (3) the Zhenpengshan granite: porphyritic medium grained; and (4) the Tianmahe granite: fine-grained (Fig. 2; Niu and Jiang, 2021b). These gneissic granites have no obvious boundaries and show gradual relationships, which display increasingly strong mylonitization and deformation towards to the Xin-Huang Fault in the southwest (Fig. 2; Liu et al., 2010).

3. Ore deposit geology

The Tongbai orogen is separated from the Dabie orogen by the Dawu Fault (Fig. 1B). The Suixian Mo deposit is situated in the core of the Tongbai complex, close to the Xin-Huan Fault (Fig. 2). The ore-bearing strata of the deposit are mainly the Neoproterozoic Tianwangzhai Group, which is mainly composed of two sections: (1) upper section: amphibolite intermingled with minor dolomite marble, and (2) lower section: leuco-gneiss (called biotite-albite leptynite and leptite by local geologists; Fig. 2). The Yaolinghe, Wudang, Doushantuo and Sigou Groups, containing schist, sandstone, and marble, are mainly in the southwestern of the area, part of a set of low-grade metamorphic rocks of greenschist facies (Fig. 2). The Caodian undeformed granite is exposed in the northeastern of the area (Fig. 2).

The Huangjiagou and Jianshuitian ore blocks are both located in the Dongyuemiao granite composed of medium-coarse grained gneissic granites with minor Augen gneissic granites (Fig. 3). The Huangjiagou ore block contains three major industrial orebodies (I, II and III) (Fig. 3A), all of which are hosted in the metamorphic rocks, especially leuco-gneiss (Fig. 4A). The exposed length and width of No. I orebody are 340 m and 10–20 m, respectively, with a Mo grade of 0.03–0.50 %. The No. II and III Mo orebodies have surface extensions of 800 m trending 310°-320°, and their total Mo ore grades are 0.03–0.50 % and 0.04 to 0.24 %, respectively (Fig. 4A; Chen et al., 2017c). The Jianshuitian ore block includes five parallel exposed orebodies with similar occurrences, and most of Mo metal resources are hosted in No. I, II and V orebodies with an average grade of 0.09 % (Fig, 4B).

The ore-host rocks include mainly leuco-gneiss and minor amphibolite with little marble (Fig. 5A-C; Fig. 6A-C). The leuco-gneiss can be divided into two-subtypes according to their biotite content and color: (1) the light colored leuco-gneiss (called leptite by local geologists) and (2) the dark colored leuco-gneiss (called leptynite by local geologists). The light colored leuco-gneiss comprises feldspar (~50 %), quartz (~45 %) and biotite (~3%) with rare amphibole and magnetite (Fig. 6A), whereas the dark colored leuco-gneiss is composed of feldspar (~40 %), quartz (~35 %), biotite (~20 %) and minor amphibole (Fig. 6B). Amphibolite is dominated by fine-grained porphyroid texture, the mineral assemblage of which includes feldspar (~40 %), amphibole (~50 %), biotite (~5%) and minor titanite (Fig. 6C). The lithology of gneissic granites (Dongyuemiao) is medium-fine grained biotite monzogranite with porphyritic (porphyroid) texture and gneissic structure (Fig. 6D).

The hydrothermal alteration at the Suixian Mo deposit consists of feldspathization with minor epidotization, chloritization, and carbonization, together with rare garnetization, tremolitization, and muscovitization (Fig. 5E-H). Feldspathization is characterized mainly by K-feldspar and albite (Fig. 5F, G), and carbonation is usually late and crosscut other alterations (Fig. 5H). The Mo mineralization types are mainly disseminated ore and fine quartz-sulfide veins. The former developed in metamorphic rocks, especially leuco-gneiss (Fig. 5A, B, L),

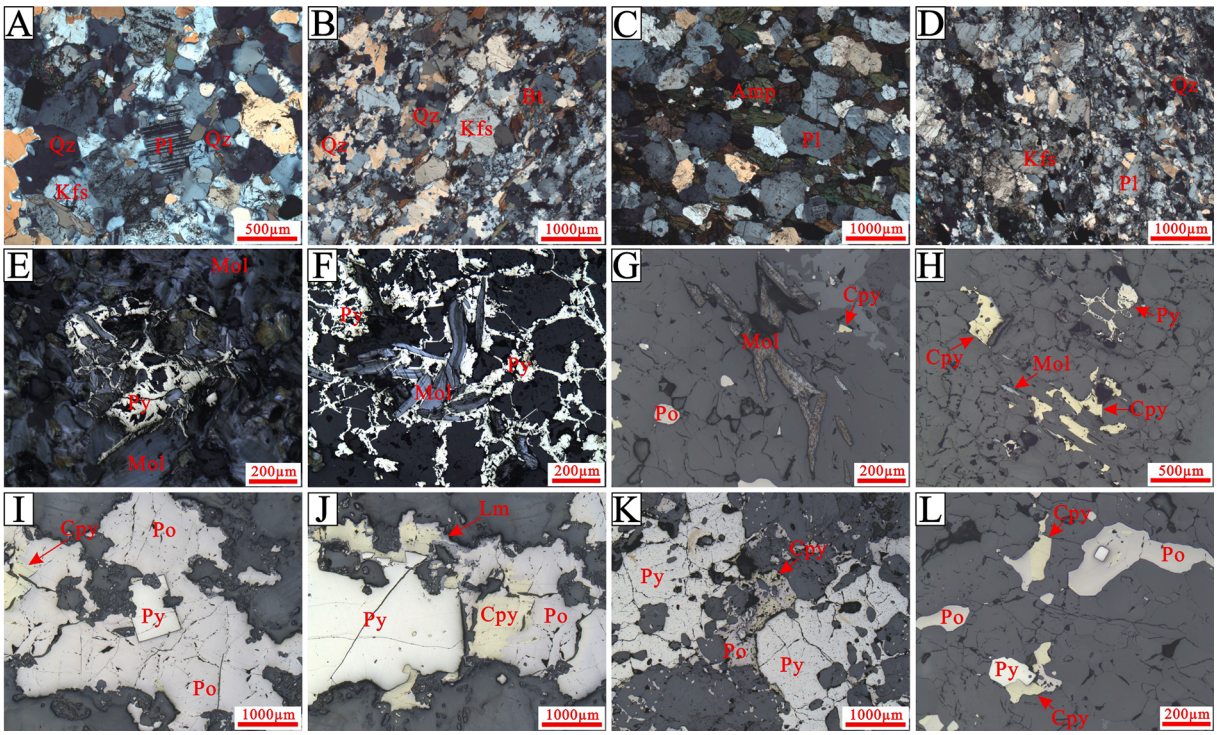

Fig. 6. Photomicrographs of walk rocks and mineralization of the Suixian Mo deposit. Photomicrograph of light colored leuco-gneiss (A), dark colored leuco-gneiss (B), amphibolite (C) and gneissic granite (D); (E-H) Molybdenite is rimmed and cross-cut by pyrite and chalcopyrite; (I-L) pyrites are often associated with or replaced by pyrrhotite and chalcopyrite, with later supergene limonite. Abbreviations: Amp- Amphibole; Bt- Biotite; Cpy- Chalcopyrite; Qz- Quartz; Pl- Plagioclase; Kfs- K-feldspar; Mol- Molybdenite; Py- Pyrite; Po- Pyrrhotite; Lm- Limonite.

and the latter occurs as Mo-bearing quartz-sulfide veins interspersed with surrounding metamorphic rocks (Fig. 5G, J, L, N). There is a small amount of scheelite mineralization in quartz-calcite veins and its economic grade is low (0.02–0.17 %; Fig. 5P).

Three hydrothermal stages were documented: (I) feldspar-quartz-amphibole-muscovite stage (Fig. 5I, J), (II) quartz-sulfides stage (Fig. 5J-N), and (III) quartz-calcite-scheelite-fluorite stage (Fig. 5O, P). Stage I veins typically contain K-feldspar, albite, quartz and minor amphibole, muscovite and scheelite, of which albite is much more abundant than K-feldspar (Fig. 5I-K). Stage II quartz-sulfide veins commonly intersperse the feldspar-quartz-amphibole-muscovite veins of stage I (Fig. 5J, K). The sulfides at stage II are mainly molybdenite, pyrite, pyrrhotite and chalcopyrite (Fig. 5J-N). Among them, molybdenite is the first to form, and is subsequently rimmed and crosscut by pyrite and chalcopyrite (Fig. 6E-H). Other euhedral pyrite crystals are commonly wrapped by pyrrhotite and chalcopyrite (Fig. 6I-L). Pyrrhotite and chalcopyrite may possibly precipitate simultaneously as their relationship is unclear (Fig. 6J, K). The quartz-calcite-fluorite veins form last and contain no molybdenite except a small amount of scheelite (Fig. 5O, P). There are some limonites and molybdites on the margin of pyrite, pyrrhotite and molybdenite, respectively, belonging to the supergene stage (Fig. 6E, J). The paragenetic relation and sequence of ore minerals and gangue minerals are shown in Fig. 7.

4. Sampling and analytical methods

4.1. Sampling

About 200 samples were collected at the Huangjiagou and Jianshuitian ore blocks, including outcrops, trenches and drilling holes. Among them, the Huangjiagou samples are mainly from the surface area of E: 113°26 ’20.22 “-113°26 ’57.00 ”, N: 32°10′ 30.32″-32°11′ 59.72″, and drilling holes of ZK1501, ZK2401, ZK002, ZK701 and ZK1601. The Jianshuitian samples are mainly from drilling holes of ZK801 and ZK1001, together with minor trenches.

We selected clean gangue minerals and ore minerals that were not affected by late hydrothermal and hypergenesis and made doubly polished thin sections. The study of fluid inclusion was based on the concept of fluid inclusion assemblage (FIA, Goldstein and Reynolds, 1994; Chi and Lu, 2008; Chi et al., 2021), and the fluid inclusions within a short trail, a cluster or a micro domain in the same crystal were treated as FIAs. We examined space distribution and location of the FIAs and the sizes, shapes, compositions and phases and proportions for individual fluid inclusions within FIAs. Thirty thin sections from three hydrothermal stages were selected for the petrographic study of fluid inclusions, and sixteen of them were used for microthermometry and laser Raman analysis. Nine typical quartz samples (three samples for each hydrothermal stage) were selected for C—H—O isotope analyses. Pyrite, pyrrhotite, chalcopyrite and molybdenite in thin sections from the quartz-sulfide veins (stage II) were selected for in situ sulfur isotope analysis. Sulfide-bearing quartz veins and metamorphic rocks, as well as gneissic granites, were selected firstly and then were ground to 40–80 mesh. The obtained samples were selected under binocular microscope to a purity of >95 %, and then ground to <200 mesh for lead isotope analysis.

4.2. Fluid inclusion analysis

Fluid inclusion petrography and subsequent microthermometric measurements, were accomplished at the Fluid Inclusion Laboratory of the Collaborative Innovation Center for Exploration of Strategic Mineral Resources of the China University of Geosciences (Wuhan). Laser Raman analysis of fluid inclusions was conducted at the State Key Laboratory of Geological Processes and Mineral Resources, China University of Geosciences (Wuhan). A Nikon Eclipse lv100pol microscope was used to study fluid inclusion petrography. The analysis for microthermometry was performed with a Leica DM2700P microscope equipped a Linkham THMS-600 with a temperature range from −196 °C to 600 °C, with

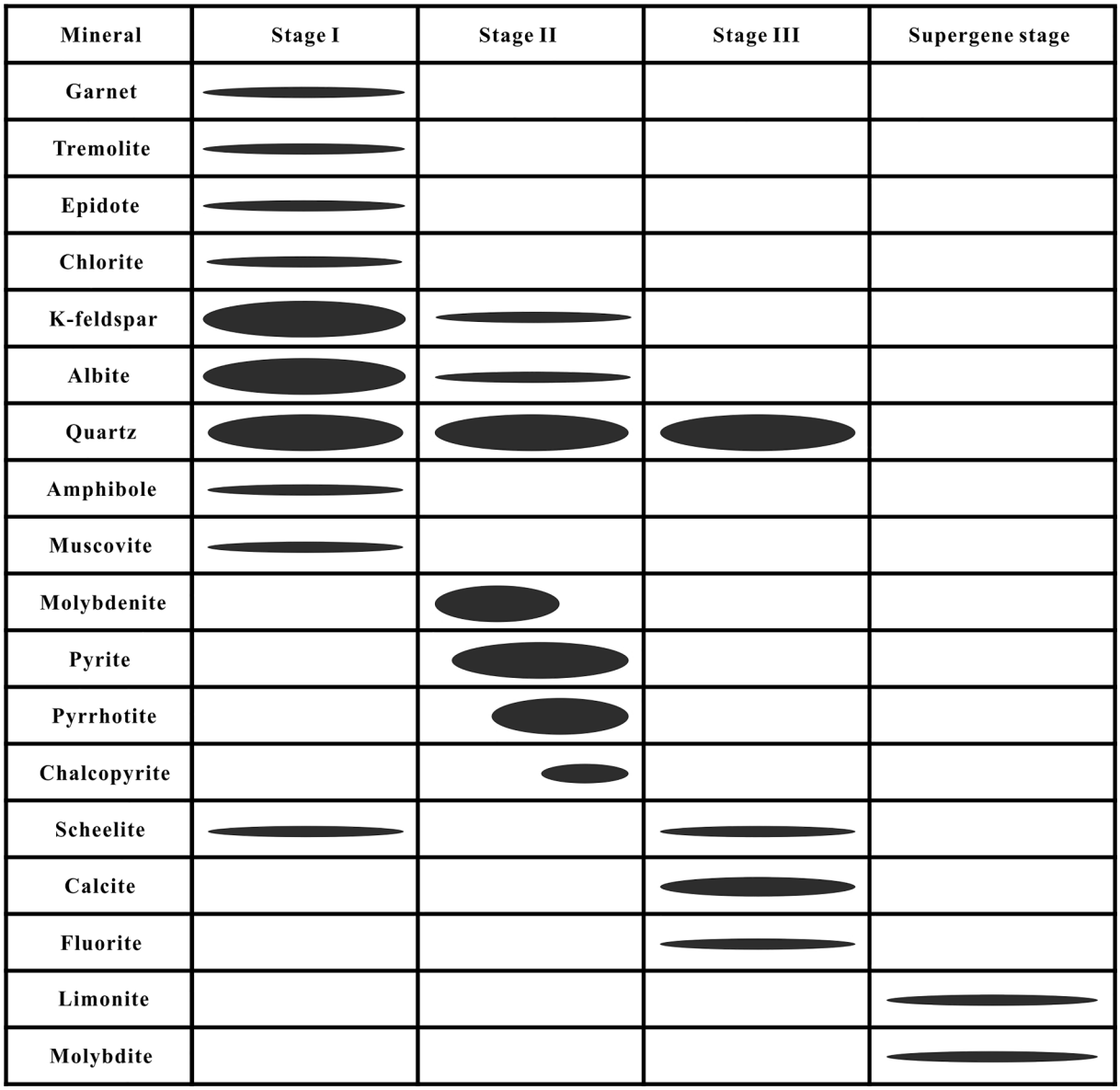

Fig. 7. Mineral paragenesis and sequence of the Suixian Mo deposit.

which a monitor and petrographic camera were connected. Before and during measurement, the above equipment was calibrated by synthetic fluid inclusions of pure aqueous and pure carbon dioxide. The rate of temperature variation for all heating and cooling processes is controlled within 20 °C/min, and <1 °C/min or <0.5 °C/min when near the phase transition point. Six temperature-related data about fluid inclusions were acquired, including ice melting ($T_{m\text{-}ice}$), first melting (T_{fm}), melting of clathrate ($T_{m\text{-}cla}$), melting of solid CO_2 ($T_{m\text{-}CO2}$), homogenization of CO_2 liquid and vapor ($T_{h\text{-}CO2}$) and total homogenization temperature (T_h). The salinities of fluid inclusions were obtained by the formula of Bodnar and Vityk (1994) for aqueous fluid inclusions and of Darling (1991) for aqueous-carbonic fluid inclusions (Schmidt and Bodnar, 2000). The laser Raman instrument for fluid inclusions was a DXR Laser Raman spectrometer with a 514.5 nm Ar + ion laser as laser source with a spectrograph aperture of 50 μm pinhole, which has a surface power of 20 MW, as well as acquisition time (10–40 s) and ranges (0–5000 cm^{-1}).

4.3. Carbon-hydrogen–oxygen isotope analysis

The C—H—O isotope analyses were carried out at the Analytical Laboratory of the Beijing Research Institute of Uranium Geology, China, using a Finnigan MAT 253 mass spectrometer. The representative quartz samples were picked out from hand specimens and ground to about 60 meshes. Separated samples were cleaned with pure 6 N nitric acid to remove other minerals and organic matter and then were repeatedly rinsed with deionized water until neutral. The obtained quartz samples were dried by heating and then were reacted with BrF_5 under vacuum conditions to release oxygen, which was collected and then converted into carbon dioxide by a platinum-plated carbon bar for oxygen isotope analysis. The pure quartz samples were heated and degassed in a quartz tube, and then were decrepitated and released mixed gas under a 500 °C vacuum condition, from which pure H_2O and CO_2 were then extracted through a collection device. The above obtained H_2O was reacted with zinc to produce H_2 for hydrogen isotope analysis, and the collected pure CO_2 was used for analysis of carbon isotopes. The above-mentioned analyses were accomplished by a gas mass spectrometer of Finnigan MAT 253, and obtained data are presented by the V-SMOW standard. The precisions of δD, $\delta^{18}O$ and $\delta^{13}C$ are ±2 ‰, ±0.2 ‰ and ±0.2 ‰, respectively. The formula for calculating oxygen isotopes of fluid through quartz is after Clayton et al. (1972): ($1000 \ln\alpha_{Quartz-H2O} = 3.38$

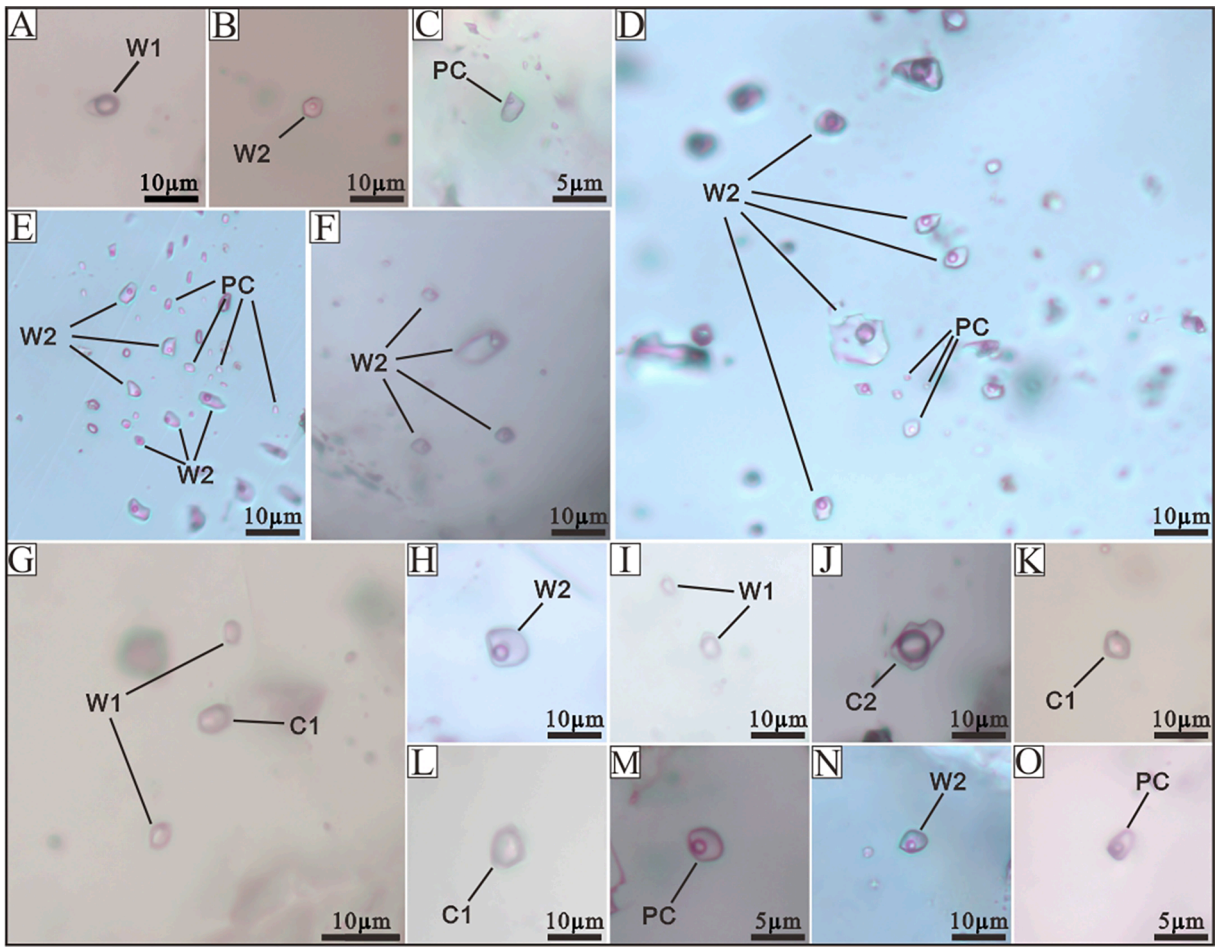

Fig. 8. Fluid inclusions petrography of different types trapped in quartz from the Suixian Mo deposit. (A-B) W1 and W2 types of fluid inclusions in stage I; (C) PC type of fluid inclusions in stage I; (D) coexisting assemblage of W2 and PC types of fluid inclusions in stage I; (E) coexisting of W2 and PC types of fluid inclusions in stage II; (F) W2 type of fluid inclusion assemblage at stage II; (G) Secondary fluid inclusion (SI) in stage II; (H-I) W1 and W2 types of fluid inclusions in stage II; (J-L) C1 and C2 types of fluid inclusions in stage II; (M) PC type of fluid inclusions in stage II; (N) W2 type of fluid inclusions in stage III; (O) PC type of fluid inclusions in stage III. Abbreviations: W1- vapor-rich two-phase aqueous fluid inclusions; W2- liquid-rich two-phase aqueous fluid inclusions; C1- three-phase CO_2-rich fluid inclusions; C2–three-phase H_2O-rich fluid inclusions; PC- two-phase pure CO_2 fluid inclusions;

$\times$ 106 T^{-2}-3.40), in which temperature (T) used is the same as the total homogenization temperatures of analyzed fluid inclusions.

4.4. Sulfur isotope analysis

The *in-situ* sulfur isotope analysis, including pyrite, pyrrhotite, chalcopyrite and molybdenite, were conducted at the Mineral Deposit Geochemistry Division of the State Key Laboratory of Geological Processes and Mineral Resources, China University of Geosciences (Wuhan), using a LA-MC-ICP-MS equipment. The used Excimer ArF laser generator can produce a deep ultraviolet beam of 193 nm, with stated parameter of the spot diameter of 23 μm, the denudation frequency of 5 Hz and the denudation time of 40 s, which was homogenized and then focused on the mineral surface for analysis. The mixed gas composed of high purity of He and Ar with minor amount of N_2, together with the denuded samples, entered into a mass spectrometer for analysis. After denudation, we obtained the $^{34}S/^{32}S$ ratio of the analyzed spot, which was used to calculate the $\delta^{34}S$ value using the SSB (standard-sample bracket) method, and there is no obvious matrix effect of different sulfides (Whitehouse et al., 2005; Zhu et al., 2017). The used standard samples during analysis include natural pyrite samples of WS-1 and WS-2, and the $\delta^{34}S$ value of WS-1 was defined either as +0.9 ‰ through gas mass spectrometer or +1.1 ‰ through SIMS, respectively (Niu et al., 2020). The corresponding analytical error (1σ) was better than ±0.1 ‰, based on the analysis of both standard and duplicate samples.

4.5. Lead isotope analysis

Lead isotope analysis for molybdenite, pyrite and pyrrhotite from ores and feldspar from gneissic granite were processed at the Analytical Laboratory of Beijing Research Institute of Uranium Geology, China. The samples were treated by the following procedures: (1) the samples were dissolved using ultrapure concentrated acids (HCl, HNO_3, HF) with heating process, and then the remaining samples were fully dissolved into dilute acid (HCl + HNO_3) and centrifuged; (2) the supernatant of the above samples was extracted and transferred into AG 1-X8 ion-exchange anion resin for lead separation; (3) The supernatant of the obtained samples was extracted and doped with standard Tl solution for analysis. The analytical instrument used was a Neptune II (MC-ICP-MS) and the obtained Pb isotope data were corrected through reference values of the NBS-981 Pb standard, with analytical reproducibility of 0.1 % (2σ) for $^{206}Pb/^{204}Pb$, $^{207}Pb/^{204}Pb$, and 0.2 % (2σ) for $^{208}Pb/^{204}Pb$ (Todt et al., 1996).

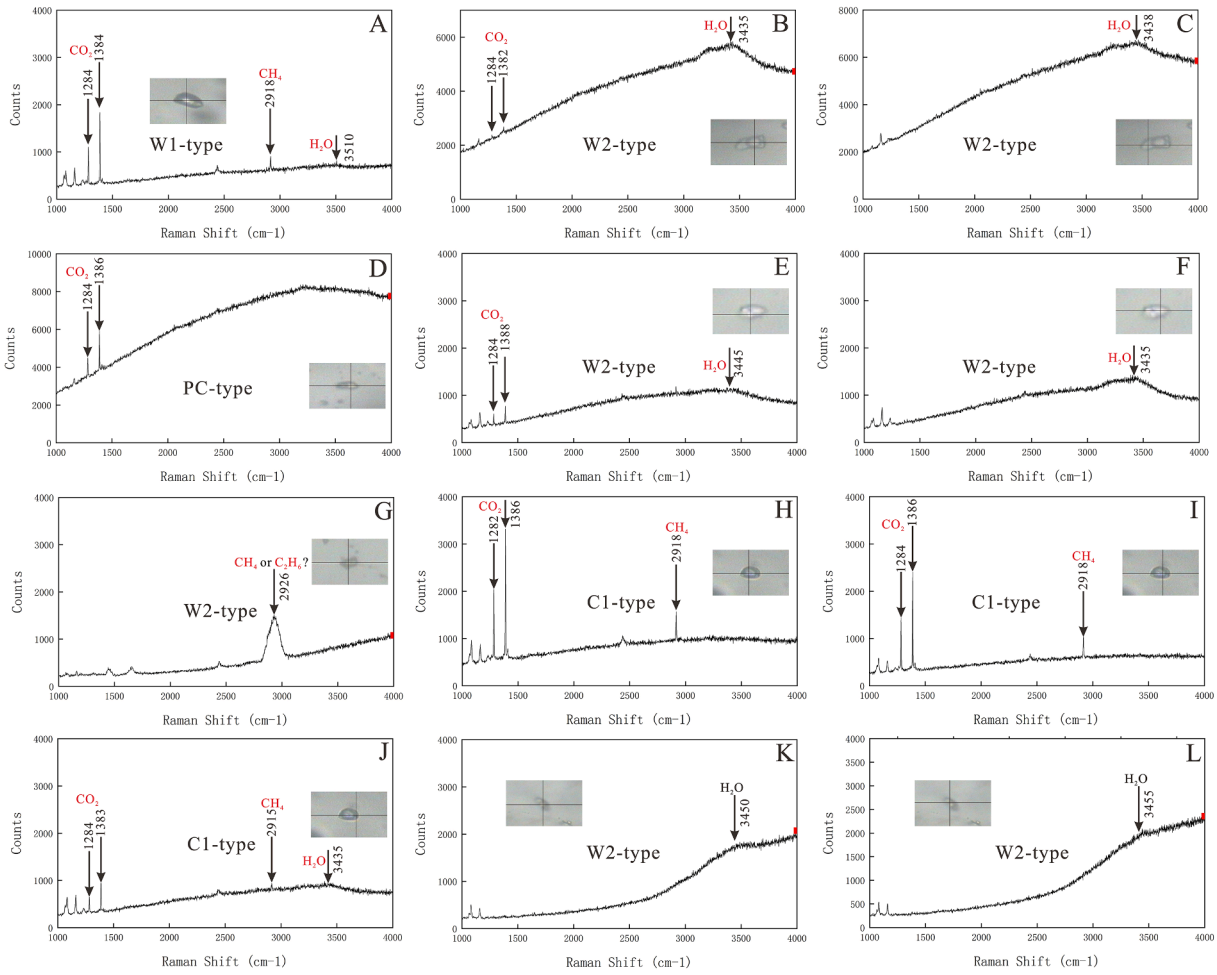

Fig. 9. Laser Raman spectra of representative fluid inclusions of W1 type (sample: ZK1501-47; A), W2 type (sample: ZK701-119; B, C) and PC type (sample: ZK1601-95; D) hosted in quartz at stage I, and fluid inclusions of W2 type (sample: ZK2401-40; E-G) and C1 type (sample: ZK1901-19; H-J) fluid inclusions at stage II, together with W2 type (sample: ZK002-8; K, L) fluid inclusions at stage III. Abbreviations: W1- vapor-rich two-phase aqueous fluid inclusions; W2- liquid-rich two-phase aqueous fluid inclusions; C1- three-phase CO_2-rich fluid inclusions; PC- two-phase pure CO_2 fluid inclusions;

5. Results

5.1. Petrography of fluid inclusions

We selected the primary (and pseudosecondary) fluid inclusions for study, based on the following criteria and procedure: (1) their distributions are regular along the growth bands of host minerals; (2) their morphology and composition are intact without deformation and leakage; (3) fluid inclusions in mineral fissures or cutting through minerals were avoided (Lu et al., 2004; Chi et al., 2017). Based on the petrographic studies, five types of fluid inclusions were recognized (at room temperature) in the studied quartz samples:

(1) Vapor-rich two-phase aqueous fluid inclusions (W1): this type of fluid inclusions contains a vapor H_2O and a liquid H_2O, and the vapor H_2O ratios are >50 vol%. The W1 types of fluid inclusions are elliptical and circular with sizes of 5–10 μm, and they mainly occur in stage I and stage II quartz (Fig. 8A, I);

(2) Liquid-rich two-phase aqueous fluid inclusions (W2): the W2 type of fluid inclusion has the same composition as the W1 type, while its volume of liquid H_2O is greater than that of vapor H_2O. This type of fluid inclusions can be seen in quartz grains of the three hydrothermal stages, and their shapes are mainly round, oval, elongated and slightly irregular with a size of 5–15 μm (Fig. 8B, D-F, H, N);

(3) Three-phase CO_2-rich fluid inclusions (C1): they comprise a liquid H_2O, a liquid CO_2 and a vapor CO_2, in which the CO_2 portion (liquid CO_2 and vapor CO_2) is between 50 and 80 vol% (Fig. 8K, L). The C1 type of fluid inclusion is nearly round and oval with sizes varying from 5 to 10 μm, and this type only occurs in stage II quartz;

(4) Three-phase H_2O-rich fluid inclusions (*C2*): similar to C1 type of fluid inclusion, the *C2* type also contains a liquid H_2O, a liquid CO_2 and a vapor CO_2, but the portion of liquid H_2O is>50 vol%. This type of fluid inclusions is usually round and nearly round with a size of 5–12 μm, and they only occur in stage II quartz (Fig. 8J);

(5) Two-phase pure CO_2 fluid inclusions (PC): they consist of one vapor CO_2 and one liquid CO_2, where the volume of the liquid CO_2 is greater than that of vapor CO_2. The PC type of fluid inclusions is found in all three hydrothermal stages, but they are small in size (3 to 6 μm; Fig. 8C, D-F, M, O). Fluid inclusion type, quantity and composition in the three stages of the Suixian Mo deposit are complex and diverse. Generally, the quartz at stage I contains W1, W2 and PC types of fluid inclusions, in which the W2 and PC types occur together and form FIAs (Fig. 8C, D), while most of W1 type of fluid inclusions are isolated (Fig. 8A). As opposed to stage I, the number of vapor-rich types of fluid inclusions at stage II (e.g., W1, C1 and *C2*) begins to increase significantly, in which the W2 and PC types of fluid inclusions commonly constitute FIAs (Fig. 8E, F), and there are also some W1 types and W1 + C1 types of FIAs at stage II (Fig. 8G, I). At stage III, the number and type of fluid inclusions decrease significantly (only W1, W2 and PC types), which are mostly distributed in isolation, relative to stages I and II (Fig. 8N, O).

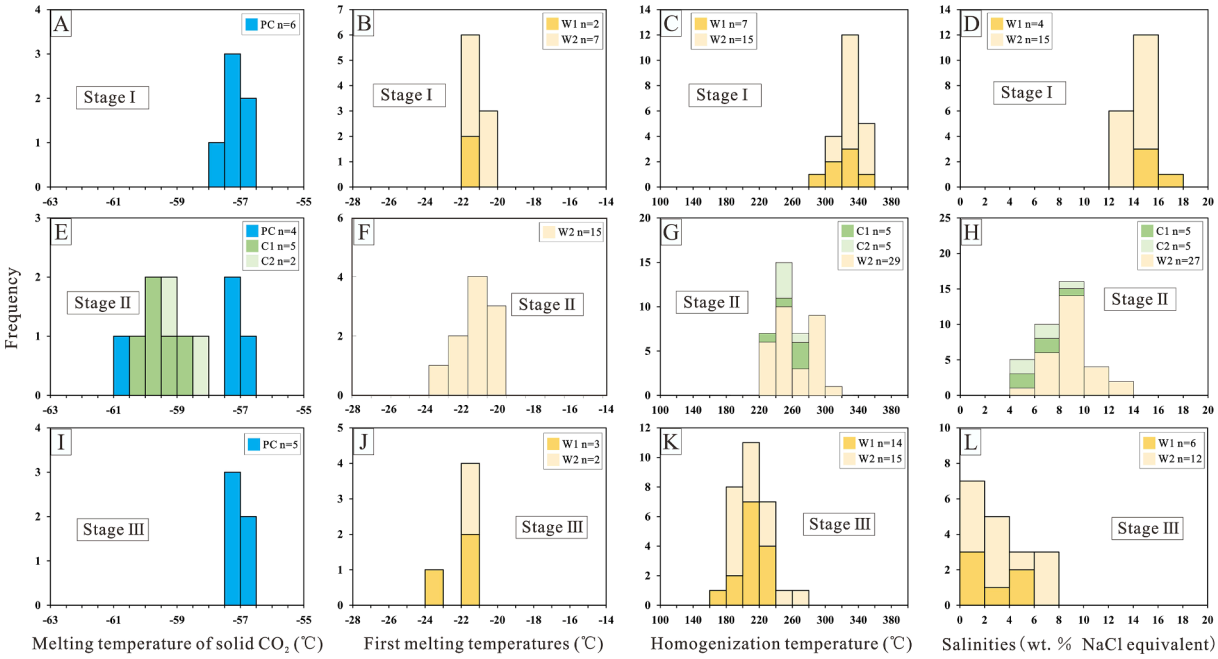

Fig. 10. Histograms of ice melting temperature ($T_{m\text{-}ice}$) and first melting temperatures (T_{fm}), as well as completely homogenization temperature (T_h) and calculated salinity of each type of fluid inclusions from stage I (A-D), stage II (E-H) and stage III (I-L) in the Suixian Mo deposit. Abbreviations: W1- vapor-rich two-phase aqueous fluid inclusions; W2- liquid-rich two-phase aqueous fluid inclusions; C1- three-phase CO_2-rich fluid inclusions; C2– three-phase H_2O-rich fluid inclusions; PC-two-phase pure CO_2 fluid inclusions;

5.2. Laser Raman spectroscopy

The W1 type of fluid inclusions in quartz of stage I shows vapor component of CO_2 (1284 and 1384 cm^{-1}), CH_4 (2918 cm^{-1}) and H_2O (3510 cm^{-1}), respectively (Fig. 9A). The vapor component of W2 type of fluid inclusions in quartz at stage I is confirmed to mainly contain H_2O with a large peak at 3435 cm^{-1}, and little CO_2 with two small peaks located at 1284 and 1382 cm^{-1}, respectively (Fig. 9B). On the other hand, the liquid phase of W2 type is mainly composed of H_2O without CO_2 (Fig. 9C). The PC type of fluid inclusions at stage I comprises CO_2 in the vapor phase as shown by the two peaks located at 1284 and 1386 cm^{-1} (Fig. 9D).

The vapor phase of W1 type of fluid inclusions at stage II contains $CO_2 + CH_4 + H_2O$ compositions, with peaks at 1284 and 1386 cm^{-1} for CO_2, as well as 2918 and 3435 cm^{-1} for CH_4 and H_2O, respectively (Fig. 9E). In the liquid phase, the composition of W1 type is mainly H_2O (Fig. 9F). Note that in the vapor phase of W2 type of fluid inclusions at stage II, a spot analysis reveals a significant peak at 2926 cm^{-1}, suggesting the presence of C_2H_6 or other organic components together with CH_4 (Fig. 9G). The C1 type of fluid inclusions in quartz of stage II yields abundant CO_2 (two peaks at 1282 and 1386 cm^{-1}) and some CH_4 (one peak at 2918 cm^{-1}) in the vapor-CO_2 phase (Fig. 9H), and the liquid-CO_2 phase shares similar feature but with less intense peaks (Fig. 9I). On the other hand, the liquid-H_2O phase contains very low signals of CO_2 and CH_4 but an intense signal of H_2O (Fig. 9J). The vapor and liquid phases of W2 type of fluid inclusion at stage III are both identified as H_2O (peak value: 3450 and 3455 cm^{-1}; Fig, 9 K, L).

5.3. Microthermometry

In total, 111 predominantly primary fluid inclusions of 35 FIAs were measured from three hydrothermal stages in the Suixian Mo deposit. According to phase relationships, there cannot be two vapor phases coexisting at any given time (Lu et al., 2004; Chi and Lu, 2008). At stage II, most of W1 type of fluid inclusions co-exist with C1 type of fluid inclusions (Fig. 8G), so these W1 type of fluid inclusions are probably

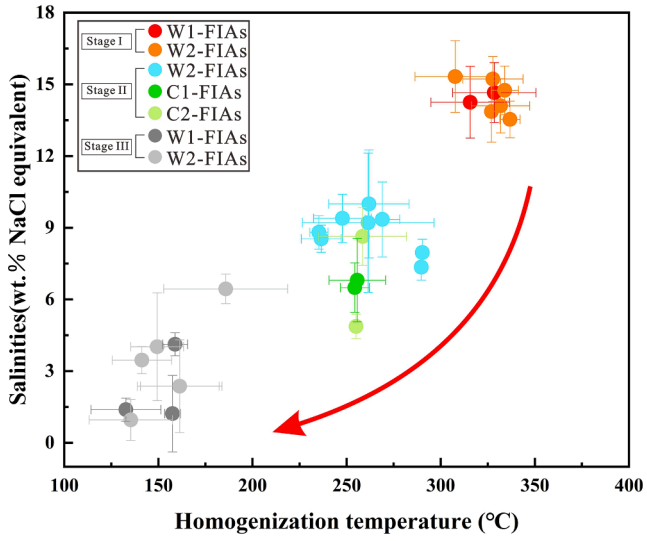

Fig. 11. Binary scatter diagram between completely homogenization temperature and salinity from fluid inclusion assemblages (FIAs) in the Suixian Mo deposit.

decrepitated and does not represent a true type of fluid inclusions. Therefore, we only conduct microthermometry on C1 type of fluid inclusions to represent the vapor phase characteristics of ore-forming fluids at stage II. The temperature data obtained for the fluid inclusions are presented in Figs. 10, 11 and listed in Table 1. Each FIA contains two to six individual fluid inclusions, in which their temperature values (tolerance of homogenization temperatures<40 °C) were averaged to represent the whole FIA. During the heating stage, all vapor-rich types of fluid inclusions (e.g., W1 and C1) homogenize to the vapor phases, while liquid-rich types of fluid inclusions (e.g., W2, *C2* and PC) homogenize to the liquid phases.

Stage I: The PC type of fluid inclusions from FIAs at this stage

Table 1
Summary for microthermometric data on fluid inclusion assemblage in the Suixian Mo deposit.

Group	Stage	FI type	N	Average (°C)							Average (wt.% NaCl eq)	
				$T_{m\text{-}CO2}$	T_{eu}	$T_{m\text{-}cla}$	$T_{h\text{-}CO2}$	$T_{m\text{-}ice}$	T_h	S. D.	Salinity	S. D.
G1	stage I	W2	4		−21.4 to −20.8 (-21.1)			−11.2 to −8.8 (-10.2)	317 to 353 (332)/L	15	12.6 to 15.2 (14.1)	1.1
G2		PC	3	−57.1 to −56.7 (-56.9)			30.6 to 31.0 (30.8)/L					
G3		W2	3		−20.9			−10.4 to −9.0 (-9.6)	331 to 341 (337)/L	5	12.8 to 14.4 (13.5)	0.8
G4		W2	3		−21.3 to −21.1 (-21.2)			−11.6 to −9.7 (-10.8)	330 to 342 (334)/L	7	13.6 to 15.6 (14.8)	1.0
G5		W2	3		−20.8			−11.9 to −10.2 (-11.3)	314 to 345 (328)/L	16	14.1 to 15.9 (15.2)	0.9
G6		W1	4		−21.4 to −21.3 (-21.4)			−10.2 to −10.3 (-10.3)	290 to 337 (316)/V	21	14.2 to 14.3 (14.3)	1.5
G7		PC	3	−57.4 to −56.8 (-57.1)			29.7 to 31.1 (30.1)/L					
G8		W1	3		−21.6			−12.4 to −10.6 (-11.5)	311 to 354 (329)/V	22	14.6 to 16.3 (15.5)	1.3
G9		W2	2		−21.7			−10.8 to −9.1 (-10.0)	327 to 328 (327)/L	1	13.0 to 14.8 (13.9)	1.3
G10		PC	2	−57.8			29.2 to 29.4 (29.3)/L					
G11		PC	2	−57.1			30.2 to 31.2 (30.7)/L					
G12	stage II	W2	6		–23.5 to −20.9 (–22.2)			−9.5 to −4.0 (-6.7)	243 to 295 (262)/L	21	6.4 to 13.4 (10.0)	2.3
G13		*C*2	2	−59.2 to −59.2 (-59.2)		7.3 to 7.7 (7.5)	26.8 to 27.1 (27)		253 to 257 (255)/L	3	4.5 to 5.2 (4.9)	0.5
G14		C1	3	−60.3 to −59.3 (-59.8)		5.5 to 7.5 (6.4)	24.5 to 28.6 (26.9)		239 to 268 (256)	15	4.9 to 8.3 (6.8)	1.7
G15		PC	3	−57.1 to −56.8 (-57.0)			26.7 to 30.5 (28.9)/L					
G16		W2	4					−5.4 to −4.5 (-5.1)	288 to 293 (290)/L	2	7.2 to 8.4 (8.0)	0.6
G17		W2	3		–22.6 to –22.6 (–22.6)			−4.9 to −4.2 (-4.6)	287 to 293 (290)/L	3	6.7 to 7.7 (7.4)	0.5
G18		C1	3	−60.3 to −58.6 (-59.3)		5.5 to 7.5 (6.5)	24.5 to 29.3 (28)		239 to 268 (254)/V	12	4.9 to 8.3 (6.5)	1.4
G19		W2	4		–22.4 to –22.4 (–22.4)			−9 to −3.5 (-6.1)	235 to 312 (261)/L	35	5.7 to 12.8 (9.2)	2.9
G20		W2	4		–22 to −21.4 (-21.7)			−7.3 to −4.9 (-6.1)	259 to 277 (269)/L	9	7.7 to 10.9 (9.4)	1.6
G21		*C*2	2	−58.2 to −58.2 (-58.2)		4.7 to 5.8 (5.3)	27.8 to 27.8 (27.8)		242 to 275 (259)/L	23	7.8 to 9.5 (8.6)	1.2
G22		W2	3		−21.9 to −20.9 (-21.4)			−6.3 to −5.3 (-5.7)	231 to 240 (235)/L	5	8.3 to 9.6 (8.8)	0.7
G23		PC	2	−60.8 to −57.3 (-59.1)			28.9 to 29.5 (29.2)/L					
G24		W2	4		−21 to −21 (−21)			−6.7 to −5.6 (-6.2)	235 to 268 (248)/L	15	8.7 to 10.1 (9.4)	1.0
G25		W2	2		−21.5 to −21.5 (-21.5)			−5.8 to −5.2 (-5.5)	229 to 244 (237)/L	11	8.1 to 8.9 (8.5)	0.6
G26	stage III	W1	4		–22.0			−1 to −0.6 (-0.8)	173 to 216 (193)/V	19	1.1 to 1.7 (1.4)	0.5
G27		W2	4		−21.3			−2.3 to −1.8 (-2.1)	187 to 223 (201)/L	16	3.1 to 3.9 (3.5)	0.6
G28		W1	6		−21.8			−2.8 to −2.2 (-2.5)	211 to 229 (219)/V	7	3.7 to 4.6 (4.1)	0.5
G29		PC	2	−57.1 to −56.8 (-57.0)			29.1 to 29.9 (29.5)/L					
G30		W1	4		–23.2			−0.7 to −0.7 (-0.7)	213 to 222 (218)/V	4	0 to 1.2 (0.3)	1.6
G31		W2	3					−0.9 to −0.2 (-0.6)	195 to 196 (195)/L	1	0 to 1.6 (1.0)	0.9
G32		PC	3	−57.3 to −56.6 (-57.0)			29.3 to 30.6 (29.9)/L					
G33		W2	3					−2.3 to −0.1 (-1.4)	202 to 246 (221)/L	22	0.2 to 3.9 (2.4)	1.9
G34		W2	3		−21.2			−3.7 to −0.9 (-2.4)	196 to 224 (209)/L	14	1.6 to 6 (4)	2.3
G35		W2	2					−4.3 to −3.7 (-4)	222.5 to 269 (246)/L	33	6 to 6.9 (6.5)	0.6

Abbreviation: W1: vapor-rich two-phase aqueous fluid inclusions; W2: liquid-rich two-phase aqueous fluid inclusions; C1: CO_2-rich three-phase fluid inclusions; *C2*: H_2O-rich three-phase fluid inclusions; PC: pure carbonic fluid inclusions; $T_{m\text{-}CO2}$: melting temperature of solid CO_2; T_{fm}: first melting temperature of aqueous fluid inclusions; $T_{m\text{-}cla}$: temperature of CO_2-clathrate dissociation; $T_{h\text{-}CO2}$: homogenization temperature of CO_2; $T_{m\text{-}ice}$: ice-melting temperature; T_h: total homogenization temperature. L: liquid phase; V: vapor phase.

demonstrates the initial melting temperatures ranging from −57.8 to −56.7 °C, which are slightly lower than the triple-point (-56.6 °C) of pure CO_2, implying the dominant CO_2 with rare other volatiles (e.g., CH_4; Fig. 10A). The corresponding complete-homogenization temperatures are from 29.2 to 31.2 °C at liquid phase. The W1 type of fluid inclusions from two FIAs yields first melting temperatures (T_{fm}) from −21.4 to −21.3 °C (Fig. 10B), approaching to the eutectic temperature of H_2O-NaCl (-20.8 °C). Meanwhile the W1 type of fluid inclusions contains ice-melting temperatures of −12.4 to −10.3 °C, with computational salinities between 14.3 and 16.3 wt% NaCl equiv. (Fig. 10D). This type of fluid inclusions homogenized to the vapor phases at temperatures of 285–354 °C (Fig. 10C).

The W2 type of fluid inclusions from five FIAs has the first melting temperatures (T_{fm}) ranging from −21.7 to −20.8 °C (Fig. 10B), close to the eutectic temperature of H_2O-NaCl (-20.8 °C). The ice-melting temperatures of W2 type of fluid inclusions are between −11.9 and −8.8 °C, corresponding to salinities from 12.6 to 15.9 wt% NaCl equiv. (Fig. 10D), and their total homogenization temperatures to liquid phases are from 314 to 353 °C (Fig. 10C).

Stage II:

The C1 type of fluid inclusions from two FIAs reveals the initial melting temperatures from −60.3 to −58.6 °C (Fig. 10E), which are significantly lower than the triple-phase point of pure CO_2 (i.e., −56.6 °C). The clathrate dissociation temperature and homogenization temperature to vapor phases of CO_2 phase are 5.5 to 7.5 °C and 24.5 to 29.3 °C, respectively (Fig. 10F). The C1 type of fluid inclusions was completely homogenized to vapor phase between 239 and 268 °C (Fig. 10G), and the calculated salinities range from 4.9 to 8.3 wt% NaCl equiv. based on the temperatures of CO_2-clathrate dissociation (5.5–7.5 °C; Fig. 10*H*). The *C2* type of fluid inclusions from FIAs shows the initial melting temperatures from −59.2 to −58.2 °C (Fig. 10E), approaching the triple-phase point of pure CO_2 (i.e., −56.6 °C). The temperatures of CO_2-clathrate dissociation for *C2* type of fluid inclusions are between 4.7 and 7.7 °C, corresponding to salinities of 4.5–9.5 wt% NaCl equiv. (Fig. 10*H*), and their complete homogenization temperatures to liquid phase are from 242 to 275 °C (Fig. 10G).

The W2 type of fluid inclusions from eight FIAs presents the first melting temperatures of –23.5 to −20.9 °C (Fig. 10F), very close to the triple-phase point temperature of NaCl (-20.8 °C), and their ice-melting temperatures are between −9.5 and −3.5 °C, with salinities of 5.7–13.4 wt% NaCl equiv. (Fig. 10H). These W2 type of fluid inclusions completely achieved liquid phase from 229 to 312 °C (Fig. 10G).

The initial melting temperatures of the PC type of fluid inclusions range from −60.8 to −56.8 °C (Fig. 10E), which are below the triple-phase point of pure CO_2 (i.e., −56.6 °C), and their homogenization temperatures range between 26.7 and 30.5 °C (Table 1).

Stage III: The PC type of fluid inclusions exhibits the initial melting temperatures of −57.3 to −56.6 °C (Fig. 10I), close to the triple-phase point of pure CO_2 of −56.6 °C, and their homogenization temperatures to liquid phase are from 29.2 to 30.6 °C (Table 1). Fourteen W1 type of fluid inclusions from three FIAs exhibit the first melting temperatures from –23.2 to −21.8 °C (Fig. 10J), and their ice-melting temperatures are between −2.8 and −0.6 °C, with salinities of 1.1 to 4.6 wt% NaCl equiv. (Fig. 10L). The fluid inclusions of W1 type were homogenized to vapor at temperatures of 173 to 229 °C (Fig. 10K). Correspondingly, fifteen fluid inclusions of W2 type from five FIAs show the first melting temperatures between −21.3 to −21.2 °C (Fig. 10J), and their ice-melting temperatures and calculated salinities are from −4.3 to −0.1 °C and 0.2 to 6.9 wt% NaCl equiv., respectively (Fig. 10L). The fluid inclusions of W2 type achieved completely uniform liquid phase at temperature of 187–269 °C (Fig. 10K).

Table 2
The C—H—O isotope data of quartz in the Suixian Mo deposit.

Mineral	$\delta^{18}O_{V\text{-}SMOW}$ (‰)	$\delta D_{V\text{-}SMOW}$ (‰)	$\delta^{13}C_{V\text{-}PDB}$ (‰)	Th (°C)	$\delta^{18}O_W$ (‰)	S. D.	Stage
Quartz	9.7	−111.2	−5.4	290 to 354	2.4 to 4.5 (3.7)	0.5	Stage I
	9.0	−109.6	−9.1		1.7 to 3.8 (3.0)		
	11.5	−114.5	−9.9		4.2 to 6.3 (5.0)		
	9.4	−101.7	−19.7	229 to 312	−1.2 to 3.1 (1.3)	1.1	Stage II
	9.8	−110	−16.8		−0.8 to 3.5 (1.7)		
	10.9	−97.6	−14.8		0.3 to 4.6 (2.8)		
	10.7	−96.8	−20.7	173 to 269	−2.9 to 2.6 (-0.4)	1.2	Stage III
	10.5	−85.5	−17.0		−3.1 to 2.4 (-0.6)		
	10.1	−87.3	−24.2		−3.5 to 2.0 (-1.0)		

Note: $\delta^{18}O_{V\text{-}SMOW}$, measured $\delta^{18}O_{V\text{-}SMOW}$ value of quartz; $\delta^{18}Ow$ value of ore-forming fluids in equilibrium with quartz is calculated according to the equation of 1000 ln $_{\alpha quartz\text{–}H2O} = 3.38 \times 106\ T^{-2} - 3.40$ reported by Clayton et al 1972. The temperatures come from the midpoint of the peak value of homogenization temperature of fluid inclusions. $\delta^{13}C_{CO2}$ values refer to CO_2 released from fluid inclusions in quartz.

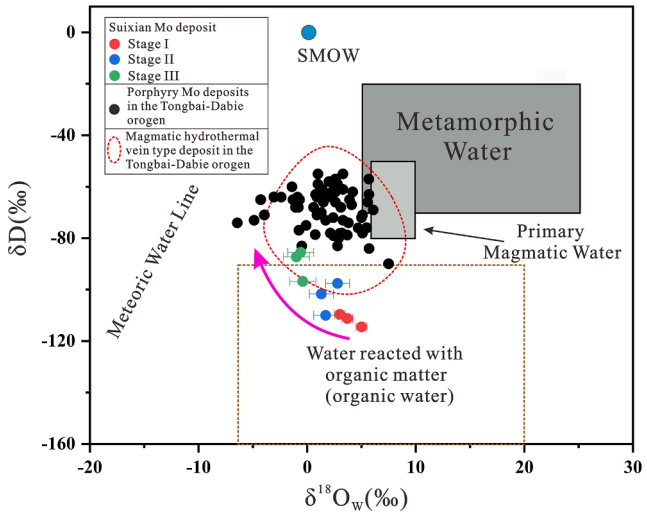

Fig. 12. Plot of $\delta^{18}O_W$ (‰) vs δD (‰) from quartz at three hydrothermal stages of the Suixian Mo deposit, also shown data for the porphyry Mo deposits in the Dabie orogen (Taylor, 1974; Yang et al., 2013; Xu et al., 2013; Wang et al., 2014b; Ni et al., 2015; Liu et al., 2017b; Niu et al., 2019; 2020).

Overall, the temperature and salinity show a clear decreasing trend from stage I, through stage II, to stage III (Fig. 11).

5.4. H—O—C isotope data

The H—O—C isotope data are listed in Table 2, including nine quartz

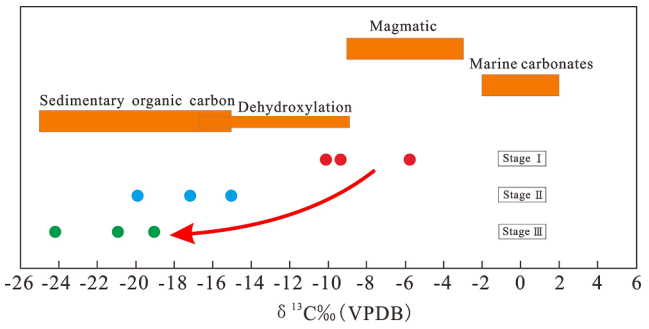

Fig. 13. Comparison of $\delta^{13}C$ values of CO_2 in the fluid inclusions trapped in quartz from three hydrothermal stages in the Suixian Mo deposit with four primary carbon sources (modified after Veizer et al., 1980; Taylor, 1986; Ohmoto, 1972).

samples from stages I, II and III, and Fig. 12 presents the results of H and O isotopes. From stage I to stage III, the $\delta D_{V\text{-}SMOW}$ values of fluid inclusions in quartz range from −115 to −110 ‰, −110 to −98 ‰ and −97 to −86 ‰, and the corresponding $\delta^{18}O_{V\text{-}SMOW}$ values of quartz are from 9.0 to 11.5 ‰, 9.4 to 10.9 ‰ and 10.1 to 10.7 ‰, respectively. Combined with the homogenization temperature of fluid inclusions in each hydrothermal stage and quartz–water fractionation equation (Table 2; Clayton et al., 1972), the oxygen isotopes of fluids ($\delta^{18}O_W$) in the three hydrothermal stages are 1.7 to 6.3 ‰ (stage I: 290 to 354 °C), −1.2 to 4.6 ‰ (stage II: 229 to 312 °C) and −3.5 to 2.6 ‰ (stage III: 173 to 269 °C), respectively.

Fig. 13 presents the C isotope results. The CO_2 presents in the fluid inclusions of quartz exhibit the $\delta^{13}C$ values of −9.9 ‰ to −5.4 ‰ (mean −8.1 ‰) at stage I, −19.7 ‰ to −14.8 ‰ (mean −17.1 ‰) at stage II, and −24.2 ‰ to −17.0 ‰ (mean −20.6 ‰) at stage III, respectively.

5.5. Sulfur isotope data

The *in-situ* sulfur isotope data including molybdenite, pyrite, chalcopyrite and pyrrhotite from stage II are listed in Table 3 and shown in Fig. 14. Most of sulfides have limited $\delta^{34}S_{V\text{-}CDT}$ values of −2.0 to 3.0 ‰, including molybdenite of −1.1 to 1.6 ‰ (mean −0.1 ‰, n = 27), pyrite of −0.8 to 2.7 ‰ (mean 1.4 ‰, n = 33), chalcopyrite of −1.7 to 0.7 ‰ (mean −0.3 ‰, n = 24) and pyrrhotite of −0.8 to 1.8 ‰ (mean 0.5 ‰, n = 16). In addition, the $\delta^{34}S_{V\text{-}CDT}$ values of a small amount of pyrite, chalcopyrite and pyrrhotite are from 9.8 to 11.2 ‰ (n = 8), while a few other pyrites exhibit low $\delta^{34}S_{V\text{-}CDT}$ values between −13.3 and −10.6 ‰ (n = 3).

5.6. Lead isotope data

The Pb isotopic compositions of molybdenite, pyrite and pyrrhotite at stage II, as well as feldspar in gneissic granite are listed in Table 4 and shown in Fig. 15. The molybdenite shows the $^{206}Pb/^{204}Pb$ ratios of 17.460 to 18.236, $^{207}Pb/^{204}Pb$ ratios from 15.422 to 15.620, and $^{208}Pb/^{204}Pb$ ratios between 37.956 and 38.507, respectively. The pyrite shows the $^{208}Pb/^{204}Pb$ ratios of 37.889–38.850, the $^{207}Pb/^{204}Pb$ ratios of 15.378–15.717 and the $^{206}Pb/^{204}Pb$ ratios of 17.239–18.483, respectively. The lead isotopic compositions of pyrrhotite show $^{206}Pb/^{204}Pb$ ratios ranging from 17.776 to 18.245, $^{207}Pb/^{204}Pb$ varying from 15.491 to 15.683 and $^{208}Pb/^{204}Pb$ changing from 37.932 to 38.706. Finally, feldspar in gneissic granite has $^{206}Pb/^{204}Pb$ ratios of 17.258–17.505, $^{207}Pb/^{204}Pb$ ratios of 15.409–15.459, and $^{208}Pb/^{204}Pb$

Table 3
Sulfur isotope data of sulfides from the Suixian Mo deposit.

Sample ID	Mineral	δ^{34}SV-CDT (‰)	Sample ID	Mineral	δ^{34}SV-CDT (‰)	Sample ID	Mineral	δ^{34}SV-CDT (‰)
ZK1001-8	Mo	−0.1	ZK1001-39	Po	0.1	ZK1901-34	Po	1.4
ZK1001-8	Mo	0.6	ZK1001-39	Po	0	ZK1901-34	Po	1.3
ZK1001-8	Mo	0.3	ZK1001-39	Po	−0.8	ZK1901-34	Po	1.6
ZK1001-8	Cpy	0.6	ZK1001-39	Po	−0.6	ZK1901-34	Po	1.8
ZK1001-8	Py	1.3	ZK1001-39	Po	−0.6	ZK1901-34	Po	1.6
ZK1001-8	Py	0.3	ZK1001-39	Po	0.3	ZK701-141	Cpy	−0.1
ZK1001-8	Py	0.6	ZK1001-39	Po	−0.6	ZK701-141	Cpy	0
ZK1001-8	Py	1.7	ZK1001-39	Py	2.0	ZK701-141	Cpy	−0.2
ZK1001-10	Mo	0.1	ZK1001-39	Py	−10.6	ZK701-141	Cpy	−0.2
ZK1001-10	Mo	0.8	ZK1001-39	Py	−11.4	ZK701-141	Cpy	0.1
ZK1001-10	Mo	0.9	ZK1001-39	Py	−13.3	ZK701-141	Cpy	−0.2
ZK1001-10	Mo	0.7	ZK1001-46	Mo	0.3	ZK1501-21	Py	1.4
ZK1001-10	Mo	1.6	ZK1001-46	Mo	0.9	ZK1501-21	Py	0.8
ZK1001-10	Mo	0.7	ZK1001-46	Mo	0.9	ZK1501-21	Py	0.4
ZK1001-16	Cpy	−1.3	ZK1001-46	Mo	0.7	ZK1501-21	Py	1.4
ZK1001-16	Cpy	−0.1	ZK1001-67	Cpy	0	ZK1501-21	Py	2.4
ZK1001-16	Cpy	−0.9	ZK1001-67	Cpy	0.1	ZK1501-21	Py	2.2
ZK1001-16	Py	−0.8	ZK1001-67	Cpy	−0.2	ZK1501-42	Py	2.6
ZK1001-16	Py	−0.6	ZK1001-67	Cpy	0.4	ZK1501-42	Py	2.7
ZK1001-16	Py	−0.4	ZK1001-67	Cpy	0.5	ZK1501-42	Py	2.7
ZK1001-16	Py	1.5	ZK1001-67	Cpy	0.7	ZK1501-42	Py	2.7
ZK1001-16	Py	1.5	ZK1901-8	Mo	0.5	ZK1501-42	Py	2.5
ZK1001-23	Mo	0.3	ZK1901-8	Mo	−0.8	ZK1501-42	Py	2.6
ZK1001-23	Mo	0.1	ZK1901-8	Mo	−0.5	ZK1701-131	Py	2.1
ZK1001-23	Mo	0.3	ZK1901-8	Mo	0.2	ZK1701-131	Py	2.3
ZK1001-23	Po	0.3	ZK1901-8	Mo	0	ZK1701-131	Py	2.3
ZK1001-23	Po	0.5	ZK1901-8	Py	−0.4	ZK1701-131	Py	2.6
ZK1001-23	Po	0.5	ZK1901-8	Py	0.4	ZK1701-131	Py	2.4
ZK1001-29	Cpy	−0.2	ZK1901-8	Py	−0.4	ZK1701-131	Py	2.4
ZK1001-29	Cpy	−0.8	ZK1901-8	Py	−0.1	ZK1501-15	Po	11.0
ZK1001-29	Cpy	−1.7	ZK1901-34	Mo	−1.1	ZK1501-15	Po	10.7
ZK1001-29	Cpy	−1.5	ZK1901-34	Mo	0	ZK1501-15	Cpy	10.7
ZK1001-29	Py	−0.6	ZK1901-34	Mo	−1.1	ZK1501-15	Cpy	10.6
ZK1001-39	Cpy	−0.7	ZK1901-34	Mo	−0.9	ZK1501-15	Cpy	9.8
ZK1001-39	Cpy	−0.8	ZK1901-34	Mo	−1.1	ZK1501-15	Po	11.0
ZK1001-39	Cpy	0	ZK1901-34	Mo	−1	ZK1501-15	Py	11.1
ZK1001-39	Cpy	0.5	ZK1901-34	Po	1.3	ZK1501-15	Py	11.2

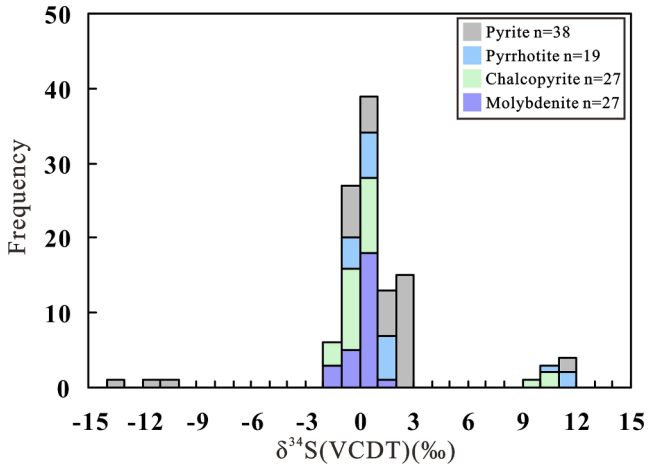

Fig. 14. Histogram of sulfur isotope values of pyrite, pyrrhotite, chalcopyrite and molybdenite at stage II from the Suixian Mo deposit.

ratios of 37.940–38.103 (Table 4).

6. Discussion

6.1. Origin of the ore-forming fluids

The C—H—O isotopes are commonly used to identify the origin of ore-forming fluids due to significant isotopic differences between magmatic, metamorphic and meteoric water (Hoefs, 2015). It is well known that the H isotope data derived from bulk analysis of fluid inclusions in quartz are very susceptible to the influence of late hydrothermal overprinting and may not accurately indicate the original fluid properties (Xiao et al., 2002). We selected pure quartz grains not altered by late hydrothermal veins for isotope analysis, and there are very few secondary fluid inclusions in long trails throughout different quartz crystals (Fig. 8D-G). Therefore, the H isotope data obtained in this study can approximately reflect the parent fluids characteristics. The homogenization temperature of fluid inclusions only represents their minimum trapping temperature except in the case of fluid immiscibility, so the calculations based on homogenization temperature for fluid oxygen isotopes may be biased from the actual situation (Chi and Lu, 2008; Chi et al., 2021). In the Suixian Mo deposit, except fluid immiscibility at stage II (will discussion later), the $\delta^{18}O_W$ at stages I and III can approximate the real fluid properties because the homogenization temperatures are equal to the trapping temperatures for an immiscible fluid system. The mean δD values of fluid inclusions in quartz exhibit a distinctly increasing tendency from −112 ‰ at stage I, through −103 ‰ at stage II, to −90 ‰ at stage III, approaching meteoric water line, which implies an increasing proportion of meteoric water in the ore-forming fluids. This is also coincident with the evolution characteristics of the $\delta^{18}O_W$ from stage I to II and III (see purple arrow in Fig. 12). It should be noted that in terms of $\delta^{18}O_W$ and δD values, the mineralizing fluids of the three stages in the Suixian Mo deposit (i.e., red, blue and green points in Fig. 12) are clearly dissociated from the typical primary magmatic water or the metamorphic water. Although the H—O isotopes in this study may be influenced by secondary fluid inclusions and calculation methods (based on homogenization temperature other than trapping temperature of fluid inclusion), it is not possible to cause these data points to deviate so much from the fields of primary magmatic water and metamorphic water, as well as typical magmatic hydrothermal vein-type deposits in the Tongbai-Dabie orogen (Fig. 12; Wang et al., 2014b; Ni et al., 2015; Liu et al., 2017b; Niu et al., 2019; 2020). Hence these mineralizing fluids cannot be derived solely from magmatic water (e.g., porphyry type deposit; Wang et al., 2021; Chen et al., 2022) or metamorphic water (e.g., orogenic deposit; Deng et al., 2020). In agreement with Fig. 12, the majority of the $\delta^{18}O_W$ and δD data in this study are in the field of water

Table 4
Results of Pb isotopic compositions of sulfides and feldspar from the Suixian Mo deposit.

Mineral	$^{208}Pb/^{204}Pb$	Std err	$^{207}Pb/^{204}Pb$	Std err	$^{206}Pb/^{204}Pb$	Std err
Molybdenite	38.188	0.005	15.587	0.003	17.871	0.005
	38.196	0.006	15.589	0.001	17.875	0.004
	38.208	0.002	15.571	0.002	17.831	0.001
	38.507	0.002	15.620	0.004	18.236	0.002
	38.406	0.018	15.497	0.007	17.823	0.008
	37.956	0.004	15.422	0.002	17.460	0.002
	38.261	0.003	15.533	0.001	17.978	0.001
	38.088	0.008	15.488	0.003	17.692	0.003
	38.324	0.003	15.554	0.001	18.063	0.001
	38.004	0.005	15.469	0.002	17.624	0.002
Pyrite	37.914	0.004	15.380	0.002	17.239	0.002
	37.889	0.004	15.378	0.001	17.266	0.002
	38.035	0.003	15.442	0.002	17.494	0.001
	38.361	0.005	15.568	0.002	18.049	0.002
	38.432	0.004	15.597	0.002	18.176	0.002
	38.423	0.004	15.643	0.002	18.147	0.002
	38.631	0.004	15.650	0.002	18.309	0.002
	38.850	0.008	15.717	0.003	18.483	0.003
	37.926	0.002	15.557	0.001	17.656	0.002
	38.029	0.002	15.515	0.001	17.565	0.002
	37.920	0.003	15.598	0.001	17.804	0.002
Pyrrhotite	38.345	0.005	15.567	0.001	18.016	0.003
	38.447	0.004	15.583	0.002	18.114	0.002
	38.706	0.004	15.683	0.002	18.245	0.002
	38.436	0.006	15.639	0.002	18.167	0.003
	37.944	0.003	15.613	0.001	17.791	0.001
	37.932	0.005	15.610	0.002	17.795	0.002
	38.375	0.004	15.651	0.002	18.233	0.002
	38.137	0.006	15.491	0.002	17.776	0.002
Feldspar in granite	38.035	0.005	15.421	0.002	17.407	0.003
	37.942	0.004	15.409	0.001	17.258	0.004
	38.103	0.006	15.459	0.002	17.505	0.002
	37.940	0.003	15.411	0.002	17.322	0.004

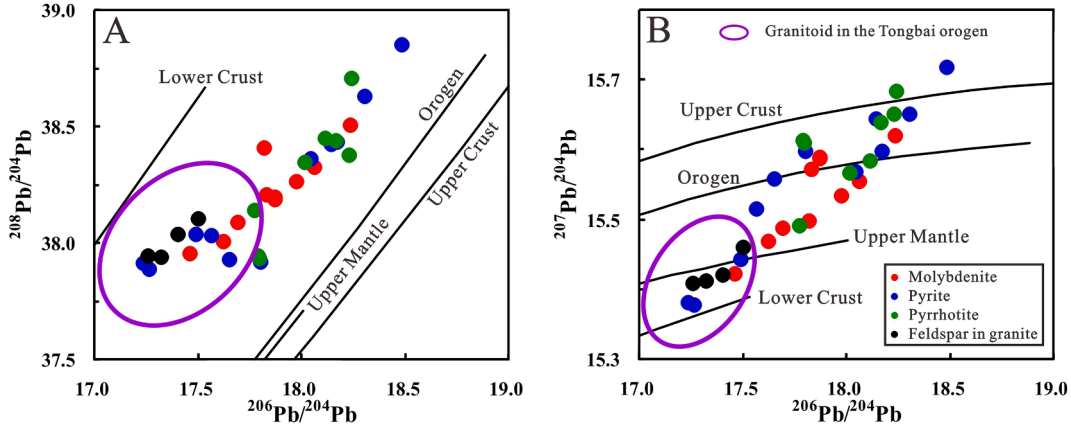

Fig. 15. Plots of Pb isotope data of molybdenite, pyrite, pyrrhotite, and feldspar in granite of the Suixian Mo deposit, also shown the data field for granitoid in the Tongbai orogen (after Niu and Jiang, 2021b and references therein).

reacted with organic matter (organic water) as defined by Hoefs (1997) and Sheppard (1986). This suggests that organic water plays a significant role in the ore-forming fluids of the Suixian Mo deposit, because primary fluid reaction with organic water results in obviously lower δD values (Fig. 12; Liu et al., 2020; Cawood et al., 2021).

The CO_2 derived from magma displays the $\delta^{13}C$ values of −9 ‰ to −3 ‰ (Taylor, 1986), whereas those originated from sedimentary organic matter and marine carbonates match values varying from −35 ‰ and −15 ‰, and approximate 0 ‰, respectively (Ohmoto, 1972; Veizer et al., 1980). Thus, the ^{13}C values of −5.4 ‰, −9.1 ‰ and −9.9 ‰ at stage I indicate that these CO_2 of fluid inclusion in quartz have a dominant magmatic source (Fig. 13). In stages II and then III, the $\delta^{13}C$ values show a progressive evolution with averages of −17.1 ‰ and −20.6 ‰, respectively, suggesting that the CO_2 in the fluids is progressively dominated by the organic carbon coming from the metasedimentary rocks (Fig. 13). Combined with fluid inclusion microthermometry and laser Raman analysis, the fluids at stage I are rich in CO_2, while the fluids at stage II have significant CH_4 in addition to CO_2 (Fig. 9 G-J; Fig. 10E). The thermochemical sulfate reduction (TSR) might have occurred when CH_4 was introduced (mixed with organic water) into the hydrothermal fluids at > 250 °C: $CH_4 + 2H^+ + SO_4^{2-} \rightarrow CO_2 + H_2S + 2H_2O$ (Hoefs, 2015), while the homogenization temperature of fluid inclusions at stage II satisfies the above conditions (229–312 °C; Fig. 10G, 11). Therefore, some CH_4 might be converted to CO_2 in the above process through mixed with organic water at stage II, resulting in a significant reduction in carbon isotopes of CO_2 (Fig. 13). These CH_4 could not possibly derive from the homochromous granitic magmatic hydrothermal fluids but leaching of metamorphic rocks in the Tongbai complex (Tianwangzhai Group), and the peripheral Wudang and Doushantuo Groups also contain a lot of organic matter, which has been demonstrated by Niu et al. (2019). Hence, the initial fluid may be magmatic hydrothermal fluid, and the mixing of organic water causes the H—O isotope data to deviate from the field of primary magmatic water (Fig. 12), and the above mixed hydrothermal fluid was as the ore-bearing fluid of the Suixian Mo deposit, in which the proportion of organic water increased from stages I to III.

6.2. Source of sulfur

The vast majority of sulfides from the Suixian Mo deposit exhibit uniform sulfur isotope feature, in which most of $\delta^{34}S$ values range from −2 ‰ to 3 ‰, and only some sulfides have more positive or negative $\delta^{34}S$ values (either < -10 ‰ or > 10 ‰),indicating that sulfides have multiple origins. Except for the few more positive (>10 ‰) and more negative (<-10 ‰) $\delta^{34}S$ values, the average sulfur isotope values for chalcopyrite, molybdenite, pyrrhotite and pyrite are −0.3 ‰, 0.1 ‰, 0.5 ‰ and 1.3 ‰, respectively, all of which are near zero. The average $\delta^{34}S$ values increase from chalcopyrite, through pyrrhotite and pyrite, to molybdenite, implying that there was an equilibrium relationship in the fluid between H_2S and sulfides (Zhang and Gao, 2012). Therefore, the sulfur isotopic characteristics of the studied sulfides can represent that of H_2S in the whole ore-forming fluid at stage II (Seal, 2006).

The sulfur from magma shows a $\delta^{34}S$ value close to 0 ‰, while that from metamorphic rocks have a large $\delta^{34}S$ range between −20 ‰ and + 20 ‰ (Jochen, 2018). Sulfides with strongly positive and negative $\delta^{34}S$ values (>10 ‰ and < -10 ‰) likely originate from the metamorphic rocks at the Suixian Mo deposit, as they are the main mineralized host rocks. On the other hand, most of the sulfides present the $\delta^{34}S$ values close to 0 ‰, which means that the deep-seated magma is most likely the main source of ore-forming materials. The magmatic hydrothermal fluid provides the dominating sulfur for sulfides with $\delta^{34}S$ values close to 0 ‰ that precipitated first. The water–rock reactions caused sulfur from the wall rocks to release to the fluids and then precipitate these sulfides with more positive or negative $\delta^{34}S$ values (Seal, 2006).

6.3. Source of lead

Molybdenite, pyrite and pyrrhotite exhibit a wide range of Pb isotopic composition, likely attesting for multiple lead sources (Table 4). In the binary scatter plot of the $^{208}Pb/^{204}Pb$ and $^{206}Pb/^{204}Pb$ (Fig. 15A), these sulfide data are restricted between the limits that correspond to the lower crust and the upper mantle. In the diagram $207Pb/^{204}Pb$ versus $^{206}Pb/^{204}Pb$ (Fig. 15B), data also spread out from lower crust, through upper mantle and orogen, to upper crust, showing a broadly linear mixing trend. The feldspar in gneissic granites and granitoid in the Tongbai orogen both show small variations in the range of lead isotopic compositions, and are closer to the lower crust and upper mantle fields (Fig. 15B). This indicates that the Pb in feldspar from gneissic granite is contemporaneous with the granitic magma from the crust but mixed with mantle materials in the Tongbai orogen, in good agreement with previous study of Niu and Jiang (2020). Thus, the Pb isotope data of feldspar in gneissic granite may represent the lead endmember of magmatic origin.

Some of the Pb isotope data for the sulfides are similar to the data for feldspar in gneissic granite, suggesting that part of the lead in this deposit has magmatic characteristics (Fig. 15A, B). In addition, the lead isotopes of sulfides show a significant trend from lower crust to the upper crustal field, suggesting that part of the lead in the upper crust was involved in the mineralization of the Suixian Mo deposit.

6.4. Fluid evolution and ore precipitation

A normal trend in fluid evolution, evidenced by steady decline in temperature and salinity, precludes strong fluid mixing in the fluid

Table 5
Comparison of characteristics between the Suixian Mo deposit and typical porphyry/orogenic-type/ magmatic hydrothermal vein type Mo deposits in the Qinling-Dabei orogenic belt (after Deng et al., 2013a, b; Niu et al., 2019; 2020; Chen et al., 2022).

		Suixian Mo deposit	Porphyry Mo deposit		Orogenic-type Mo deposit	Magmatic hydrothermal vein type deposit
Molybdenum mineralization age		Cretaceous (131–137 Ma)	Triassic	Jurassic-Cretaceous	Precambrian (~1850 Ma) and Triassic (218–244 Ma)	~1.76 Ga, ~0.85 Ga and Triassic
Geologic setting		post-collisional	continental arcs	post-collisional	continental collision or subduction-related accretion orogenies	post-collisional
Hydrothermal alteration		epidotization, chloritization, garnetization, tremolite alteration, feldspathization (K-feldspar and albite), carbonization	phyllic, propylitic, and argillic alteration	potassic alteration and silicification	K-feldspar, sericitization, fluoritization, and carbonation	K-feldspar, sericitization, and carbonation
Ore-bearing strata (rocks)		Precambrian metavolcanic rocks	monzogranite, granite porphyry	K-feldspar granite, biotite granite, and monzogranite	Huaxiong block	Surrounding metamorphic rock
Ore-forming fluid	**temperature**	163–354 °C	109–341 °C	97–550 °C	210–550 °C	100–500 °C
	salinity	0.2–17.3 wt% NaCl. Eq.	0.2–11.8 wt% NaCl. Eq.	0.5–54 wt% NaCl. Eq.	0.8–44 wt% NaCl. Eq.	1.0–45 wt% NaCl. Eq.
	composition	CO_2 -rich and abundant CH_4	CO_2 -poor	CO_2 -rich	CO_2 -rich and minor CH_4 or N_2	CO_2 -rich (minor CH_4)
	fluid inclusions	L + V, L + V + CO_2	L + V	L + V, L + V + CO_2, L + V + S	L + V, L + V + CO_2, minor L + V + S	L + V, L + V + CO_2, L + V + S
	origin	magmatic fluid	magmatic fluid	magmatic fluid	metamorphic fluids surrounding rock or basement	magmatic fluid
Ore-forming materials		magma	magma	magma		magma
Ore forming mechanism		fluid mixing/immiscibility	fluid boiling	fluid immiscibility	fluid immiscibility	fluid mixing/ immiscibility

evolution of this deposit (Fig. 11). Combined with the C—H—O isotopes, fluid mixing may be a continuous mixing of organic water and meteoric water from stages I to III (Fig. 12; Ni et al., 2015). Organic matter made an important contribution in many types of mineral deposits, such as orogenic deposits (Wu et al., 2020), porphyry deposits (Peng et al., 2018) and sediment-hosted deposits (Leach et al., 2010). At higher temperatures (>120 °C), organic matter enters into the ore-bearing fluid and the following thermochemical sulfate reaction (TSR) will take place: (1) $SO_4^{2-} + 2C \rightarrow S^{2-} + 2CO_2$, (2) $SO_4^{2-} + CH_4 \rightarrow H_2S + CO_3^{2-} + H_2O$ and (3) $SO_4^{2-} + 2CH_2O \rightarrow H_2S + 2HCO_3^-$ (Worden et al., 1995; Leach et al., 2005; Zhou et al., 2013). Given the high levels of CH_4 in fluid at stage II, the above reaction (2) was probably the most important reaction (Fig. 9D-I), leading to an increasing H_2S concentrations and react with metal ions (e.g., Mo, Fe, Cu) in the fluid. This process resulted in the fluid transform from oxidizing to reducing, which is proved by a large amount of cogenetic pyrrhotite (Fig. 6I-L; Schrader et al., 2021). Experiments show that molybdenum is transported in the fluid in the form of $MoO(OH)_2Cl$ (+5) or $(HMoO_4)^-$ (+6), and precipitates as molybdenite when converted to tetravalence (Cao, 1989; Bali et al., 2012; Hurtig et al., 2021). The thermochemical sulfate reaction caused by the mixed organic matter not only produces a large amount of reduced sulfur (S^{2-}), but also reduces the valence of molybdenum in the fluid, making it easier to precipitate as molybdenite.

There are distinct CO_2 in the fluid at stages I and II (Fig. 9A, C-G), and it is clear that these CO_2 at stage I were mainly derived from magmatic hydrothermal fluids (Fig. 13). We hypothesize that fluid immiscibility occurred from stages I to II, as evidenced by the following facts: (1) inhomogeneous capture of fluid inclusions: W2 type fluid inclusions (liquid phase) and PC type (vapor phase) coexist in an FIA (Fig. 8D, E), and (2) phase separation: liquid (W2 and *C*2 types) and vapor (C1 type) phases have similar homogenization temperatures (Fig. 10G, 11; Wang et al., 2015; Li et al., 2020; Chi et al., 2021). Fluid immiscibility results in decreasing temperature and enrichment of ore metals in fluid, which creates favorable ore-forming conditions (Wang et al., 2021). In addition, the escape of CO_2 from the fluid decrease H^+ concentration with the following reaction: $H^+ + HCO_3^- \rightarrow H_2O + CO_2$, $H_2S \rightarrow H^+ + HS^-$ and $HS^- \rightarrow H^+ + S^{2-}$, leading to the enrichment of reduced sulfur (S^{2-}) and reduction of Mo solubility in the fluid (Kaszuba et al., 2006; Bali et al., 2012).

Therefore, the mixed organic water and fluid immiscibility, as well as the participation of meteoric water, decrease temperature and Mo solubility, and increase the concentration of reduced sulfur (S^{2-}) in fluid, leading to the precipitation of molybdenite in the Suixian Mo deposit.

6.5. Ore genesis

Some researchers classified the Suixian Mo deposit as a porphyry deposit because of the contemporaneous granite and molybdenite occurrence in the veinlets (Chen et al., 2017a; Niu et al., 2017; Dai et al., 2018). Combined with previous isotope dating results, the Suixian Mo ores deposited at 131–137 Ma (Re-Os age of molybdenite; Niu et al., 2017; Chen et al., 2017c), which is similar or slightly later than the gneissic granite in the Tongbai complex (138–144 Ma, U-Pb age of zircon; Liu et al., 2010; Zhang et al., 2018; Niu and Jiang, 2021b). No porphyry rocks (may relate to porphyry-type Mo deposit) occur in the Suixian Mo deposit other than the gneissic granite. Typical porphyry deposit comprises well-organized alteration zonations from potassiumization and propylitization to sericinization and argillization (Kerrich et al., 2000; Cook, 2005; Sillitoe, 2010), while such alteration zonations in the Suixian Mo deposit were not present except for some local and minor propylitization, feldspar (K-feldspar and albite) and carbonization (Fig. 7). The H—O isotope data are obviously different from those of porphyry Mo deposits in the Dabie area (Fig. 12; Yang et al., 2013; Xu et al., 2013; Wang et al., 2014b; Ni et al., 2015; Liu et al., 2017b), hence the hypothesis that the Suixian Mo deposit pertains to porphyry-type deposit is less likely. Together with C—H—O—S—Pb isotope data, the initial fluid in the Suixian Mo deposit is magmatic hydrothermal in the early stage (I), with which organic matter (e.g., CH_4) in metamorphic rocks and meteoric water were mixed as ore-forming fluid at later stages (II, III). Furthermore, part of the hydrothermal alterations (propylitization, K-feldspathization and garnetization) are also the product of high-temperature magmatic hydrothermal activity. Therefore, fluid system of the Suixian Mo deposit should be magmatic hydrothermal fluids mixing with organic water derived from the host metamorphic

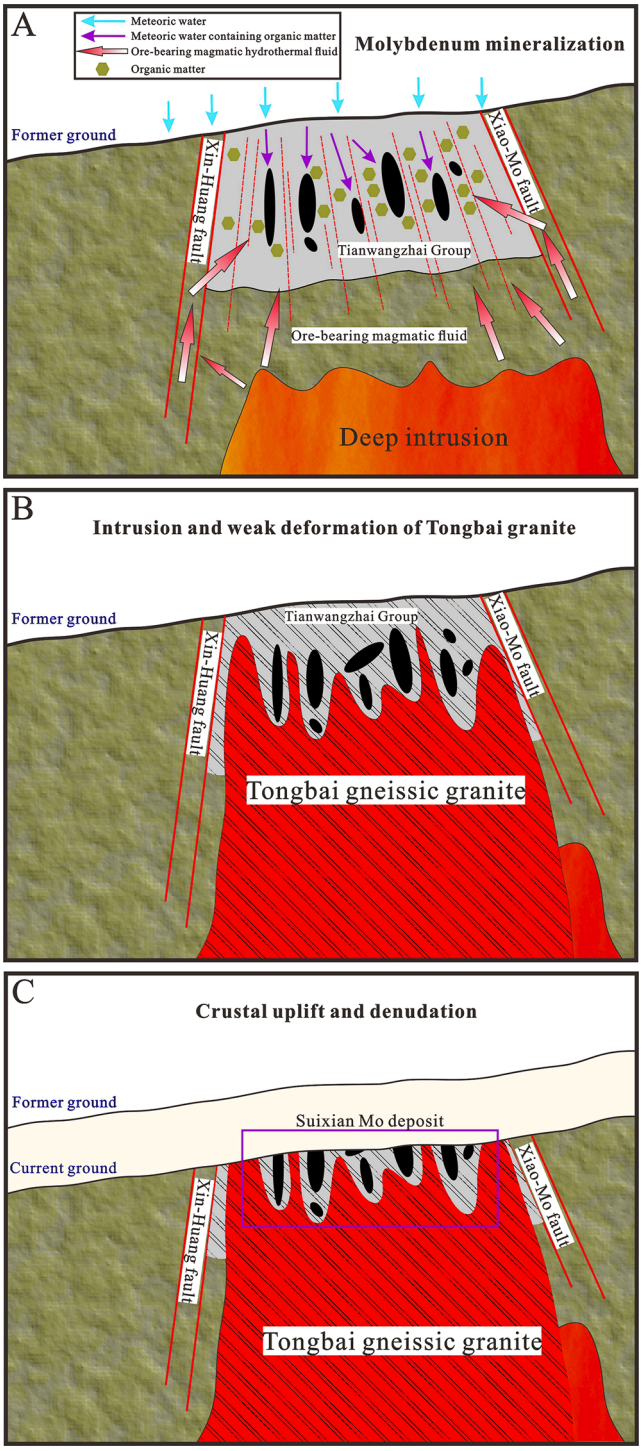

Fig. 16. Schematic diagram to explain the forming process of the Suixian Mo deposit. (A) the ore-bearing hydrothermal fluid from deep intrusion caused molybdenum mineralization in the Tianwangzhai Group, (B) the Tongbai granite intruded and regional weak deformation, and (C) crustal uplift and denudation.

rocks, different from the porphyry-type and orogenic-type Mo deposits in the Qinling-Dabei orogenic belt (Table 5; Goldfarb et al., 2001, 2005; Goldfarb and Groves, 2015; Groves et al., 2003; Chen et al., 2022).

In addition to porphyry (skarn) and orogenic deposits, there are also some magmatic hydrothermal vein-type deposits in the Qinling-Dabie orogen, characterized by (1) they are usually distributed in the periphery of intrusions; (2) the orebodies mainly occur in surrounding rocks rather than within the intrusions; (3) their initial ore-bearing fluid is magmatic hydrothermal; (4) the mineralization types are mainly veins and disseminated; (5) the mineralization process is obviously controlled by faults; (6) fluid immiscibility or mixing is an important ore-forming mechanism, for example the Zhaiwa Mo-Cu deposit and Tumen Mo-fluorite deposit in the Qinling orogen (e.g., Deng et al., 2013a,b; Chen et al., 2022), and the Zaopa Mo-Ag deposit and Wangjiadashan Mo-Cu deposit in the Tongbai-Dabie orogen (e.g., Niu et al., 2019; 2020). Therefore, the Suixian Mo deposit can be defined as a magmatic hydrothermal vein-type deposit related to intrusions. Nevertheless, molybdenum mineralization is not closely related to the cotemporaneous gneissic granitic intrusions (Dongyuemiao granite), implying that the formation of the Suixian Mo deposit may be related to concealed intrusions at depth (Wu et al., 2015; Xiang et al., 2017). We conclude that a contemporary cogenetic magmatic rock (deep intrusion) provided the mineralizing fluids for the Suixian Mo deposit (Fig. 16A). These fluids circulated along the Xin-Huang Fault and the Xiao-Mo Fault, as well as their secondary faults, and mixed with organic waters that may originate from meteoric water circulated in the Tainwangzhai Group, leading to the precipitation of Mo orebodies in the Tiangwangzhai Group (Fig. 16A). Subsequently, the granite from the Tongbai complex intruded into the Tianwangzhai Group and encapsulated these ore-bearing metamorphic rocks as enclaves (Fig. 16B), and then shearing and deformation produced the gneissic granite, which underwent late surface denudation due to crustal uplift (Fig. 16C).

7. Conclusions

1. The Mo mineralization of the Suixian deposit all occurred in the metamorphic rocks of the Tianwangzhai Group, and the current exploration did not reveal any direct contact with the surrounding gneissic granite in the Tongbai complex.
2. The ore-forming fluid is a medium–high temperature, medium–low salinity fluid rich in CO_2 and CH_4.
3. The C—H—O isotope data prove that the initial ore-bearing fluid is dominantly magmatic fluid, but mixed with organic fluid that originated from meteoric water interacted with the organic matter enriched host metamorphic rocks.
4. The S-Pb isotopic data indicate that the ore-forming materials are mainly from magma and mixed with upper crustal materials (surrounding rocks).
5. Thermochemical sulfate reaction caused by the mixed organic matter and fluid immiscibility are two important ore-forming mechanisms.
6. The Suixian Mo deposit is a magmatic hydrothermal vein-type deposit related to intrusions rather than a porphyry or skarn deposit.

Declaration of Competing Interest

The authors declare that they have no known competing financial interests or personal relationships that could have appeared to influence the work reported in this paper.

Data availability

All the data are in the tables of this paper

Acknowledgements

We appreciate Prof. Zhao Kuidong and Ms. Liu Mu for their help during isotopic analysis. Mr. Chen Qizhi is thanked during fluid inclusion study. This research is financially supported by grants from the National Natural Science Foundation of China (No. 42030811), the State Key Laboratory of Geological Processes and Mineral Resources of China University of Geosciences (no. MSFGPMR03-2). Thanks to the associate editor for detailed handing and two anonymous reviewers for constructive suggestions.

References

Bali, E., Keppler, H., Audetat, A., 2012. The mobility of W and Mo in subduction zone fluids and the Mo–W–Th–U systematics of island arc magmas. Earth Planet Sci. Lett. 351–352, 95–207.

Bodnar, R.J., Vityk, M.O., 1994. Interpretation of microthermometric data for H_2O-NaCl fluid inclusions. In: De Vivo, B., Frezzotti, M.L. (Eds.), Fluid inclusions in Minerals, Methods and Applications: Blacksburg. Virginia Polytechnic Institute and State University, Virginia, pp. 117–130.

Cao, X., 1989. Solubility of molybdenite and the transport of molybdenum in hydrothermal solutions. In: Retrospective Theses and Dissertations. Iowa State University, pp. 1–103.

Cao, M.P., Yao, J.M., Deng, X.H., Yang, F.J., Mao, G.Z., Mathur, R., 2016. Diverse and multistage Mo, Au, Ag-Pb-Zn and Cu deposits in the Xiong'er terrane. East Qinling: from Triassic Cu mineralization. Ore Geol. Rev. 81, 565–574.

Cawood, I.P., Murphy, J.B., McCarthy, W.J., Boyce, A.J., 2021. O and H isotopic evidence for a mantle source of water in appinite magma: An example from the late Neoproterozoic Greendale Complex, Nova Scotia. Lithos 386–387, 105997.

Chen, Q.Z., Jiang, S.Y., Duan, R.C., 2017c. The geochemistry, U-Pb and Re-Os geochronology, and Hf isotopic constraints on the genesis of the Huangjiagou Mo deposit and related granite in the Dabie region, Hubei Province. China. Ore Geol. Rev. 81, 504–517.

Chen, Y.J., Pirajno, F., Li, N., Deng, X.H., 2017a. Molybdenum deposits in China. Ore Geol. Rev. 81, 401–404.

Chen, Y.J., Wang, P., Li, N., Yang, Y.F., Pirajno, F., 2017b. The collision-type porphyry Mo deposits in Dabie Shan, China. Ore Geol. Rev. 81, 405–430.

Chen, Y.J., Pirajno, F., Li, N., Deng, X.H., Yang, Y.F., 2022. Geology and geochemistry of molybdenum deposits in the Qinling Orogen, P R China. Modern Approaches Solid Earth Sci. 22 https://doi.org/10.1007/978-981-16-4871-7_1.

Chi, G., Diamond, L.W., Lu, H., Lai, J., Chu, H., 2021. Common problems and pitfalls in fluid inclusion study: a review and discussion. Minerals 11, 1–17.

Chi, G., Haid, T., Quirt, D., Fayek, M., Blamey, N., Chu, H., 2017. Petrography, fluid inclusion analysis, and geochronology of the End uranium deposit, Kiggavik. Nunavut. Canada. Mineral. Deposita. 52, 211–232.

Chi, G., Lu, H., 2008. Validation and representation of fluid inclusion microthermometric data using the fluid inclusion assemblage (FIA) concept. Acta Petrol. Sin. 9, 1945–1953.

Clayton, R.N., O'Neil, J.R., Mayeda, T.K., 1972. Oxygen isotope exchange between quartz and water. J. Geophys. Res. 77, 3057–3067.

Cook, D.K., 2005. Giant porphyry deposits: characteristics, distribution, and tectonic controls. Econ. Geol. 100, 801–818.

Cui, J.J., Liu, X.C., Dong, S.W., Hu, J.M., 2012. U-Pb and $^{40}Ar/^{39}Ar$ geochronology of the Tongbai complex, central China: Implications for Cretaceous exhumation and lateral extrusion of the Tongbai-Dabie HP/UHP terrane. J. Asian Earth Sci. 47, 155–170.

Dai, S.J., Xiang, X.H., Chen, Z.W., Feng, J.L., Wang, J.J., 2018. Stable isotopic characteristics of Huangjiagou-Jiangshuitian molybdenum deposit in Suixian and their significance. Resour. Environ. Eng. 32, 341–344 in Chinese with English abstract.

Darling, R.S., 1991. An extended equation to calculate NaCl contents from final clathrate melting temperatures in H_2O-CO_2-NaCl fluid inclusions: Implications for P-T, isochore location. Geochim. Cosmochim. Acta 55, 3869–3871.

Deng, X.H., Chen, Y.J., Santosh, M., Yao, J.M., 2013a. Re-Os geochronology, fluid inclusions and genesis of the 0.85Ga Tumen molybdenite-fluorite deposit in Eastern Qinling, China: implications for pre-Mesozoic Mo enrichment and tectonic setting. Geol J 48, 484–497.

Deng, X.H., Chen, Y.J., Santosh, M., Yao, J.M., 2013b. Genesis of the 1.76Ga Zhaiwa Mo-Cu and its link with the Xiong'er volcanics in the North China Craton: implications for accretionary growth along the margin of the Columbia supercontinent. Precambrian Res. 227, 337–348.

Deng, X.H., Chen, Y.J., Pirajno, F., Li, N., Yao, J.M., Sun, Y.L., 2017. The geology and geochronology of the Waifangshan Mo-quartz vein cluster in Eastern Qinling, China. Ore Geol. Rev. 81, 548–564.

Deng, J., Yang, L.Q., Groves, D.I., Zhang, L., Qiu, K.F., Wang, Q.F., 2020. An integrated mineral system model for the gold deposits of the giant Jiaodong province, eastern China. Earth-Sci. Rev 208, 103274.

Gao, Y., Mao, J.W., Ye, H.S., Li, F.L., Li, Y.F., Luo, Z.Z., Xiong, B.K., Meng, F., 2014. Geochronology, geochemistry and Sr-Nd-Pb isotopic constraints on the origin of the Qian'echong porphyry Mo deposit, Dabie orogen, east China. J. Asian Earth Sci. 85, 163–177.

Gao, Y., Mao, J.W., Ye, H.S., Li, Y.F., Luo, Z.Z., Yang, Z.Q., 2016. Petrogenesis of ore-bearing porphyry from the Tangjiaping porphyry Mo deposit, Dabie orogen: zircon U-Pb geochronology, geochemistry and Sr-Nd-Hf isotopic constraints. Ore Geol. Rev. 79, 288–300.

Gao, Y., Mao, J.W., Ye, H.S., Li, Y.F., 2018. Origins of ore-forming fluid and material of the quartz-vein type Mo deposits in the East Qinling-Dabie molybdenum belt: a case study of the Qianfanling Mo deposit. J. Geochem. Explor. 185, 52–63.

Goldfarb, R.J., Baker, T., Dube, B., Groves, D.I., Gart, C.J.R., Gosselin, P., 2005. Distribution, character, and genesis of gold deposits in metamorphic terranes. Econ. Geol. 100th Anniversary Volume 407–450.

Goldfarb, R.J., Groves, D.I., 2015. Orogenic gold: Common or evolving fluid and metal sources through time. Lithos 233, 2–26.

Goldfarb, R.J., Groves, D.I., Gardoll, S., 2001. Orogenic gold and geologic time; a global synthesis. Ore Geol. Rev. 18, 1–75.

Goldstein, R.H., Reynolds, T.J., 1994. Systematics of fluid inclusions in diagenetic minerals. Soc. Sediment. Geol. Short Course 31, 199.

Groves, D.I., Goldfarb, R.J., Robert, F., Hart, C.J.R., 2003. Gold deposits in metamorphic belts: overview of current understanding, outstanding problems, future research, and exploration significance. Econ. Geol. 98, 1–29.

He, Y.S., Li, S.G., Hoefs, J., Huang, F., Liu, S.A., Hou, Z.H., 2011. Post-collisional granitoids from the Dabie orogen: new evidence for partial melting of a thickened continental crust. Geochim. Cosmochim. Acta 75, 3815–3838.

He, Y.S., Li, S.G., Hoefs, J., Kleinhanns, I.C., 2013. Sr-Nd-Pb isotopic compositions of Early Cretaceous granitoids from the Dabie orogen: constraints on the recycled lower continental crust. Lithos 156–159, 204–217.

Hoefs, J., 1997. Stable Isotope Geochemistry. Springer, Berlin/Heidelberg, pp. 1–201.

Hoefs, J., 2015. Stable Isotope Geochemistry, Seventh Edition. Springer, Cham, pp. 1–389.

Hurtig, N., Migdisov, A.A., Williams-Jones, A.E., 2021. Are vapor-like fluids viable ore fluids for Cu-Au-Mo porphyry ore formation? Econ. Geol. 116, 1599–1624.

Jochen, H., 2018. Stable Isotope Geochemistry, Eighth ed. Springer International Publishing AG, Switzerland, pp. 1–336.

Kaszuba, J.P., Williams, L., Janecky, D.R., Hollis, W.K., Tsimpanogiannis, I.N., 2006. Immiscible CO_2-H_2O fluids in the shallow crust. Geochem. Geophys. Geosyst. 7, 1–11.

Kerrich, R., Goldfarb, R., Groves, D., Garwin, S., 2000. The characteristics, origins, and geodynamic settings of supergiant gold metallogenic provinces. Sci. China Ser. D: Earth Sci. 43, 1–68.

Leach, D.L., Sangster, D.F., Kelley, K.D., et al., 2005. Sediment-hosted lead-zinc deposits: a global perspective. Econ. Geol. 100th Anniversary Volume 561–607.

Leach, D.L., Bradley, D.C., Huston, D., Pisarevsky, S.A., Taylor, R.D., Gardoll, S.J., 2010. Sediment-hosted lead-zinc deposits in Earth history. Econ. Geol. 105, 593–625.

Li, N., Chen, Y.J., Santosh, M., Pirajno, F., 2018. Late Mesozoic granitoids in the Qinling Orogen, Central China, and tectonic significance. Earth-Sci. Rev. 182, 141–173.

Li, X.H., Klyukin, Y.I., Steele-Maclnnis, M., Fan, H.R., Yang, K.F., Zoheir, B., 2020. Phase equilibria, thermodynamic properties, and solubility of quartz in saline-aqueous-carbonic fluids: Application to orogenic and intrusion-related gold deposits. Geochim. Cosmoch. Ac. 283, 201–221.

Liu, X.C., Jahn, B.M., Cui, J.J., Li, S.Z., Wu, Y.B., Li, X.H., 2010. Triassic retrograded eclogites and Cretaceous gneissic granites in the Tongbai Complex, central China: implications for the architecture of the HP/UHP Tongbai-Dabie-Sulu collision zone. Lithos 119, 211–237.

Liu, X., Li, S.Z., Suo, Y.H., Liu, X.C., Dai, L.M., Santosh, M., 2011. Structural anatomy of the exhumation of high-pressure rocks: constraints from the Tongbai collisional orogen and surrounding units. Geol. J. 46, 156–172.

Liu, Q.Q., Li, B., Shao, Y.J., Lu, A.H., Lai, J.Q., Li, Y.F., Luo, Z.Z., 2017a. Molybdenum mineralization related to the Yangtze's lower crust and differentiation in the Dabie Orogen: evidence from the geochemical features of the Yaochong porphyry Mo deposit. Lithos 282–283, 111–127.

Liu, Q.Q., Shao, Y.J., Li, Y.F., Luo, Z.Z., 2017b. Processes and ore genesis at the Yaochong Mo deposit, Henan Province, China. Ore Geol. Rev. 86, 692–706.

Liu, G.X., Yuan, F., Deng, Y.F., Wang, F.Y., White, N.C., Huizenga, J.M., Li, Y., Li, X.H., Zhou, T.F., 2020. Ore-fluid geochemistry of the Hehuashan Pb-Zn deposit in the Tongling ore district, Anhui province, China: evidence from REE and C-H-O isotopes of calcite. Ore Geol. Rev. 117, 103279.

Lu, H.Z., Fan, H.R., Ni, P., Ou, G.X., Shen, K., Zhang, W.H., 2004. Fluid Inclusion. Science Press, Beijing, pp. 1–487 (in Chinese with English abstract).

Mao, J.W., Pirajno, F., Xiang, J.F., Gao, J.J., Ye, H.S., Li, Y.F., Guo, B.J., 2011. Mesozoic molybdenum deposits in the east Qinling-Dabie orogenic belt: characteristics and tectonic settings. Ore Geol. Rev. 43, 264–293.

Mi, M., Chen, Y.J., Yang, Y.F., Wang, P., Li, F.L., Wan, S.Q., Xu, Y.L., 2015a. Geochronology and geochemistry of the giant Qian'echong Mo deposit, Dabie Shan, eastern China: implications for ore genesis and tectonic setting. Gondwana Res. 27, 1217–1235.

Mi, M., Li, C.Y., Sun, W.D., 2015b. Qian'echong low-F porphyry Mo deposits in the Dabie Mountains, central China. Lithos 239, 157–169.

Ni, Z.Y., Chen, Y.J., Li, N., Zhang, H., 2012. Pb-Sr-Nd isotope constraints on the fluid source of the Dahu Au-Mo deposit in Qinling orogen, central China, and implication for Triassic tectonic setting. Ore Geol. Rev. 46, 60–67.

Ni, Z.Y., Li, N., Zhang, H., 2014. Hydrothermal mineralization at the Dahu Au–Mo deposit in the Xiaoqinling gold field, Qinling orogen, central China. Geol. J. 49, 501–514.

Ni, P., Wang, G.G., Yu, W., Chen, H., Jiang, L.L., Wang, B.H., Zhang, H.D., Xu, Y.F., 2015. Evidence of fluid inclusions for two stages of fluid boiling in the formation of the giant Shapinggou porphyry Mo deposit, Dabie orogen, central China. Ore Geol. Rev. 65, 1078–1094.

Niu, Z.Y., Feng, J.L., Xiang, X.H., Zhang, C., Lv, X.Z., 2017. The Re-Os isochron isotope age of Huangjiagou molybdenum deposits and its geological significance in Suixian, Hubei Province. Resour. Environ. Eng. 31, 683-387 (in Chinese with English abstract).

Niu, P.P., Jiang, S.Y., 2021b. Geochronological, geochemical, and Sr-Nd-Pb-Hf isotopes of Cretaceous gneissic granite and quartz monzonite in the Tongbai Complex: Record of lower crust thickening beneath the Tongbai orogen. Geol. J 1–24. https://onlinelibrary.wiley.com/doi/10.1002/gj.4154.

Niu, P.P., Jiang, S.Y., Xiong, S.F., Hu, Q.S., Xu, T.L., 2019. Geological characteristics, fluid inclusions and H-O-C-S isotopes of the Zaopa Ag-Mo prospect in the Suizao area, Hubei Province: Implications for ore genesis. Ore Geol. Rev. 111, 103012.

Niu, P.P., Jiang, S.Y., 2020. Petrogenesis of the Late Mesozoic Qijinfeng Granite Complex in the Tongbai orogen: Geochronological, geochemical and Sr-Nd-Pb-Hf isotope evidence. Lithos 356–357, 105290.

Niu, P.P., Jiang, S.Y., Hu, Q.S., Xu, T.L., Xiong, S.F., 2020. Fluid inclusions and H-O-C-S isotope constraints on fluid evolution and ore genesis of the Wangjiadashan Cu-Au

deposit in Suizao area of the Tongbai-Dabie orogenic belt, central China. Geol. J. 55, 1563–1586.
Niu, P.P., Jiang, S.Y., 2021a. Geochemistry, zircon U-Pb geochronology, and Hf isotopes of the metavolcanic rocks in the Tongbai orogen of central China: Implication for Neoproterozoic oceanic subduction to slab break-off. Precambrian Res. 361, 106239.
Ohmoto, H., 1972. Systematics of sulfur and carbon isotopes in hydrothermal ore deposits. Econ. Geol. 67, 551–578.
Peng, N.J., Jiang, S.Y., Xiong, S.F., Pi, D.H., 2018. Fluid evolution and ore genesis of the Dalingshang deposit, Dahutang W-Cu ore field, northern Jiangxi Province, South China. Mineral. Deposita 53, 1079–1094.
Ren, Z., Zhou, T.F., Hollings, P., White, N.C., Wang, F.Y., Yuan, F., 2018. Trace element geochemistry of molybdenite from the Shapinggou superlarge porphyry Mo deposit, China. Ore Geol. Rev. 95, 1049–1065.
Schmidt, C., Bodnar, R.J., 2000. Synthetic fluid inclusions: XVI. PVTX properties in the system H_2O-NaCl-CO_2, at elevated temperatures, pressures, and salinities. Geochim. Cosmochim. Acta 64, 3853–3869.
Schrader, D.L., Davidson, J., McCoy, T.J., Zega, T.J., Russell, S.R., Domanik, K.J., King, A.J., 2021. The Fe/S ratio of pyrrhotite group sulfides in chondrites: an indicator of oxidation and implications for return samples from asteroids Ryugu and Bennu. Geochim. Cosmochim. Acta 303, 66–91.
Seal, R.R.I., 2006. Sulfur isotope geochemistry of sulfide minerals. Rev. Mineral. Geochem. 61, 633–677.
Sheppard, S.M.F., 1986. Characterization and isotopic variations in natural waters. In: Valley, J.W., Taylor, H.P., O'Neil, J.R. (Eds.), Stable Isotopes. Reviews in Mineralogy and Geochemistry, 165-181.
Sillitoe, R.H., 2010. Porphyry copper systems. Econ. Geol. 105, 3–41.
Taylor, H., 1974. The application of oxygen and hydrogen isotope studies to problems of hydrothermal alteration and ore deposition. Econ. Geol. 69, 843–883.
Taylor, B.E., 1986. Magmatic volatiles: isotopic variation of C, H, and S. Rev. Mineral. 16, 185–225.
Todt, W., Cliff, R.A., Hanser, A., Hofmann, A.W., 1996. Evaluation of a ^{202}Pb-^{205}Pb double spike for high-precision lead isotope analysis. Geophys. Monograph. Ser. 95, 429–437.
Veizer, J., Holser, W.T., Wilgus, C.K., 1980. Correlation of $^{13}C/^{12}C$ and $^{34}S/^{32}S$ secular variations. Geochim. Cosmochim. Acta 44, 579–587.
Wang, Y., Chen, Y., Ma, H.W., Xu, Y.L., 2009. Study on ore geology and fluid inclusions of the Tangjiaping Mo deposit, Shangcheng country, Henan province. Acta Petrol. Sin. 25, 468–480 in Chinese with English abstract.
Wang, P., Chen, Y.J., Fu, B., Yang, Y.F., Mi, M., Li, Z.L., 2014b. Fluid inclusion and H-O-C isotope geochemistry of the Yaochong porphyry Mo deposit in Dabie Shan, China: a case study of porphyry systems in continental collision orogens. Int. J. Earth Sci. 103, 777–797.
Wang, G.G., Ni, P., Yu, W., Chen, H., Jiang, L.L., Wang, B.H., Zhang, H.D., Li, P.F., 2014a. Petrogenesis of Early Cretaceous post-collisional granitoids at Shapinggou, Dabie Orogen: implications for crustal architecture and porphyry Mo mineralization. Lithos 184–187, 393–415.
Wang, P., Wang, Y., Yang, Y.F., 2017. Zircon U-Pb geochronology and isotopic geochemistry of the Tangjiaping Mo deposit, Dabie Shan, eastern China: implications for ore genesis and tectonic setting. Ore Geol. Rev. 81, 466–483.
Wang, Z.L., Yang, L.Q., Guo, L.N., Marsh, E., Wang, J.P., Liu, Y., Zhang, C., Li, R.H., Zhang, L., Zheng, X.L., Zhao, R.X., 2015. Fluid immiscibility and gold deposition in the Xincheng deposit, Jiaodong Peninsula, China: a fluid inclusion study. Ore. Geol. Rev. 65, 701–717.
Wang, S.W., Zhou, T.F., Hollings, P., Yuan, F., Fan, Y., White, N.C., Zhang, L.J., 2021. Ore genesis and hydrothermal evolution of the Shaxi porphyry Cu-Au deposit, Anhui province, Eastern China: evidence from isotopes (S-Sr-H-O), pyrite, and fluid inclusions. Mineral. Deposita 56, 767–788.
Whitehouse, M.J., Kamber, B.S., Fedo, C.M., Lepland, A., 2005. Integrated Pb- and S-isotope investigation of sulphide minerals from the early Archaean of southwest Greenland. Chem. Geol. 222, 112–131.
Worden, R.H., Smalley, P.C., Oxtoby, N.H., 1995. Gas souring by the thermo chemical sulfate reduction at 140°C. AAPG Bull. 79, 854–863.
Wu, Y.F., Evans, K., Fisher, L.A., Zhou, M.F., Hu, S.Y., Fougerouse, D., Large, R.R., Li, J. W., 2020. Distribution of trace elements between carbonaceous matter and sulfides in a sediment-hosted orogenic gold system. Geochim. Cosmochim. Acta 276, 345–362.
Wu, Y.B., Wang, H., Gao, S., Hu, Z.C., Liu, X., Gong, H.J., 2014. LA-ICP-MS monazite U-Pb age and trace element constraints on the granulite-facies metamorphism in the Tongbai orogen, central China. J. Asian Earth Sci. 82, 90–102.
Wu, X.L., Zhang, C., Hu, Q.S., Gui, H.Z., 2015. Discussion on geological characteristics and genesis of Huangjiagou-Jiangshuitian molybdenum deposit. Resour. Environ. Eng. 29, 790–794 in Chinese with English abstract.
Xiang, X.H., Dai, S.J., Niu, Z.Y., Feng, J.L., Wang, J.J., 2017. Geochemical characteristics and genetic analysis of molybdenum deposits in Huangjiagou. Resour. Environ. Eng. 31, 675–682 in Chinese with English abstract.
Xiang, X.H., Chen, Y.C., Li, Y.L., Li, F., Wang, Q., 2019. Geochemical characteristics, age and genesis of granite in Tongbai Complex, Northern Suizhou-Zaoyang. Resour. Environ. Eng. 33, 454–459 in Chinese with English abstract.
Xiao, Y.L., Hoefs, J., Van Den Kerkhof, A.M., Simon, K., Fiebig, J., Zheng, Y.F., 2002. Fluid evolution during HP and UHP metamorphism in Dabie Shan, China: constraints from mineral chemistry, fluid inclusions and stable isotopes. J. Petrol. 43, 1505–1527.
Xu, Z.W., Liu, S.M., Chen, W., Zuo, C.H., Li, H.C., Yang, X.N., Wang, H., Yang, Q.Y., 2013. An isotopic geochemical study on the Dayinjian molybdenum deposit, Xinxian County, Henan Province. Geogr. Rev. 59, 983–992 in Chinese with English abstract.
Yang, Y.F., Chen, Y.J., Li, N., Mi, M., Xu, Y.L., Li, F.L., Wan, S.Q., 2013. Fluid inclusion and isotope geochemistry of the Qian'echong giant porphyry Mo deposit, Dabie Shan, China: a case of NaCl-poor, CO_2-rich fluid systems. J. Geochem. Explor. 124, 1–13.
Yang, Y.F., Wang, P., Chen, Y.J., Li, Y., 2017. Geochronology and geochemistry of the Tianmugou Mo deposit, Dabie Shan, eastern China: implications for ore genesis and tectonic setting. Ore Geol. Rev. 81, 484–503.
Zhang, H.F., Gao, S., 2012. Geochemistry. Geological Publishing House, Beijing, pp. 1–410 in Chinese.
Zhang, J.Y., Ma, C.Q., She, Z.B., Zhang, C., 2013. Geochronology and geochemistry of the Early Cretaceous Jigongshan and Qijianfeng batholiths in the Tongbai orogen, central China: implications for lower crustal delamination. Int. J. Earth Sci. 104, 1045–1067.
Zhang, W.X., Zhu, L.Q., Wang, H., Wu, Y.B., 2018. Generation of post-collisional normal calc-alkaline and adakitic granites in the Tongbai orogen, central China. Lithos 296–299, 513–531.
Zhou, J.X., Huang, Z.L., Zhou, M.F., et al., 2013. Constraints of C-O-S-Pb isotope compositions and Rb-Sr isotopic age on the origin of the Tianqiao carbonate-hosted Pb-Zn deposit, SW China. Ore Geol. Rev. 53, 77–92.
Zhu, Z.Y., Jiang, S.Y., Ciobanu, C.L., Yang, T., Cook, N.J., 2017. Sulfur isotope fractionation in pyrite during laser ablation: implications for laser ablation multiple-collector inductively coupled plasma mass spectrometry mapping. Chem. Geol. 450, 223–234.